

Modeling CO Emission: II. The Physical Characteristics that Determine the X factor in Galactic Molecular Clouds

Rahul Shetty¹, Simon C. Glover¹, Cornelis P. Dullemond^{1,2}, Eve C. Ostriker³,
Andrew I. Harris³, Ralf S. Klessen¹

¹ *Zentrum für Astronomie der Universität Heidelberg, Institut für Theoretische Astrophysik, Albert-Ueberle-Str. 2, 69120 Heidelberg, Germany*

² *Max Planck Institut für Astronomie, Königstuhl 17, 69117 Heidelberg, Germany*

³ *Department of Astronomy, University of Maryland, College Park, MD, 20742, USA*

Accepted 2011 April 18. Received 2011 April 15; in original form 2011 February 24

ABSTRACT

We investigate how the X factor, the ratio of the molecular hydrogen column density (N_{H_2}) to velocity-integrated CO intensity (W), is determined by the physical properties of gas in model molecular clouds (MCs). The synthetic MCs are results of magneto-hydrodynamic simulations, including a treatment of chemistry. We perform radiative transfer calculations to determine the emergent CO intensity, using the large velocity gradient approximation for estimating the CO population levels. In order to understand why observations generally find cloud-average values of $X = X_{\text{Gal}} \sim 2 \times 10^{20} \text{ cm}^{-2} \text{ K}^{-1} \text{ km}^{-1} \text{ s}$, we focus on a model representing a typical Milky Way MC. Using globally integrated N_{H_2} and W reproduces the limited range in X found in observations and a mean value $X = X_{\text{Gal}} = 2.2 \times 10^{20} \text{ cm}^{-2} \text{ K}^{-1} \text{ km}^{-1} \text{ s}$. However, we show that when considering limited velocity intervals, X can take on a much larger range of values due to CO line saturation. Thus, the X factor strongly depends on both the range in gas velocities, as well as the volume densities. The temperature variations within individual MCs do not strongly affect X , as dense gas contributes most to setting the X factor. For fixed velocity and density structure, gas with higher temperatures T has higher W , yielding $X \propto T^{-1/2}$ for $T \sim 20 - 100 \text{ K}$. We demonstrate that the linewidth-size scaling relationship does not influence the X factor – only the *range* in velocities is important. Clouds with larger linewidths σ , regardless of the linewidth-size relationship, have a higher W , corresponding to a lower value of X , scaling roughly as $X \propto \sigma^{-1/2}$. The “mist” model, often invoked to explain a constant X_{Gal} consisting of optically thick cloudlets with well-separated velocities, does not accurately reflect the conditions in a turbulent molecular cloud. We propose that the observed cloud-average values of $X \sim X_{\text{Gal}}$ is simply a result of the limited range in N_{H_2} , temperatures, and velocities found in Galactic MCs – a nearly constant value of X therefore does not require any linewidth-size relationship, or that MCs are virialized objects. Since gas properties likely differ (albeit even slightly) from cloud to cloud, masses derived through a standard value of the X factor should only be considered as a rough first estimate. For temperatures $T \sim 10 - 20 \text{ K}$, velocity dispersions $\sigma \sim 1 - 6 \text{ km s}^{-1}$, and $N_{\text{H}_2} \sim 2 - 20 \times 10^{21} \text{ cm}^{-2}$, we find cloud-averaged values $X \sim 2 - 4 \times 10^{20} \text{ cm}^{-2} \text{ K}^{-1} \text{ km}^{-1} \text{ s}$ for Solar-metallicity models.

Key words: ISM:clouds – ISM: lines and bands – ISM: molecules – ISM: structure – line:profiles – stars:formation

1 INTRODUCTION

Carbon monoxide (CO), the second most abundant molecule in the interstellar medium (ISM), has now been observed for over thirty years to investigate the physical characteristics

of the ISM. The lowest rotational levels are easily excited through collisions with molecular hydrogen (H_2), by far the primary component of molecular gas in the ISM. Since H_2 is difficult to detect directly, and the ^{12}CO J=1-0 line oc-

curs at a frequency (115.27 GHz) that is readily observable from Earth, CO observations are well suited for probing the conditions of the molecular component of the ISM.

Accurately measuring the masses and velocities of gas within molecular clouds (MCs) is of primary importance for understanding star formation. CO observations of Galactic and extra-galactic MCs have provided a wealth of information about these properties, allowing for detailed modeling of the star formation process. However, uncertainty remains about exactly how to convert observed CO emission into fundamental physical properties of the dominant molecular component of the ISM.

The low rotational transition lines of CO are known to be optically thick, and therefore a considerable fraction of the emission from high density regions must be self-absorbed. Nevertheless, a strong correlation is found between the CO intensity and the H_2 column density N_{H_2} . A number of methods are employed to measure N_{H_2} . These include mass determinations using observations of ^{13}CO , which has lower optical depth than ^{12}CO and so may be capable of tracing much of the MC gas (e.g. Dickman 1978). Alternatively, if MCs are in virial equilibrium, the ^{12}CO linewidth may be used to estimate the virial mass (e.g. Larson 1981; Solomon et al. 1987). Independent mass measurements not involving CO include observations of γ -rays, which are produced when cosmic rays interact with the ISM. The molecular content is deduced when HI observations provide information about the amount of atomic material along the line-of-sight (Strong et al. 1988). Dust-based observations in the infrared may also provide indirect gas mass estimates, using appropriate dust-to-gas ratios (e.g. Dame et al. 2001; Pineda et al. 2008; Leroy et al. 2009).

The correlation between ^{12}CO ($J=1-0$)¹ intensity W and N_{H_2} is expressed as

$$X = \frac{N_{H_2}}{W} \text{ (cm}^{-2} \text{ K}^{-1} \text{ km}^{-1} \text{ s)}. \quad (1)$$

In the Milky Way, observational analyses generally find this “ X factor” to be nearly constant and $\sim \text{few} \times 10^{20} \text{ cm}^{-2} \text{ K}^{-1} \text{ km}^{-1} \text{ s}$, hereafter X_{Gal} , for both MCs (see e.g. Solomon et al. 1987; Young & Scoville 1991, and references therein) and the lower density diffuse ISM (e.g. Polk et al. 1988; Liszt et al. 2010). In regions with very high molecular densities, such as ultraluminous infrared galaxies (ULIRGs), X is found to be ~ 1 -5 times lower than X_{Gal} . There is believed to be only a small range in the X factor among ULIRGs (see Solomon & Vanden Bout 2005, and references therein). As a result suitable X factors, depending on environment, are commonly used for directly estimating the N_{H_2} (or gas mass) from CO observations.

A key assumption in using an X factor to derive gas masses is that the CO line is an approximately linear tracer of the bulk of the MC gas. Since the CO line is optically thick, however, it is not obvious why a linear relationship should hold. Extending the analysis of Dickman et al. (1986), Solomon et al. (1987) advanced the “mist” model in which a MC is composed of optically thick cloudlets that have well separated velocities, such that the amount of self-absorption in the MC is small, and W is proportional to the total number of cloudlets along the line-of-sight, hereafter

LoS. The assumptions implicit to this “mist” model have not, however, been tested with radiative transfer modeling in realistic MC models.

Despite the correlations between W and N_{H_2} described above, there are in fact signs that no universal X factor is applicable to all sources. First, since the CO line is optically thick, observations of Galactic MCs show that beyond a threshold column density, W saturates so that the CO line no longer traces gas mass (Lombardi et al. 2006; Pineda et al. 2008). Observations of low metallicity systems such as the SMC suggest $X \gg X_{\text{Gal}}$ (Israel et al. 1986; Israel 1997; Boselli et al. 1997, 2002; Leroy et al. 2009, 2011). Theoretically, low metallicity systems are expected to have lower CO abundances, which lead to lower CO intensities and thereby larger X factors (Maloney & Black 1988; Wolfire et al. 1993; Israel 1997; Shetty et al. 2011) provided that the other properties of the MCs (e.g. mass, size) do not vary greatly with metallicity (Glover & Mac Low 2011). Further, using independent dust-based measures of N_{H_2} leads to X factor estimates that differ from X computed through the “virialized” cloud assumption (Bolatto et al. 2008; Leroy et al. 2007, 2009). This discrepancy is taken as evidence that there are large reservoirs of molecular gas untraced by CO (Grenier et al. 2005; Planck Collaboration et al. 2011). One explanation for such a situation is that in the outer regions of MCs, CO cannot form efficiently due to poor self-shielding (Wolfire et al. 2010).

The discrepancies and range in the X factor estimates need to be understood in order to accurately interpret CO observations. One important issue related to the X factor is the dynamical state of MCs. Two well known scaling relationships for MCs have been established in large part due to CO observations: the mass-size and linewidth-size relationships (Larson 1981), often referred to colloquially as “Larson’s Laws.” Assuming constant X , the MC masses M are found to be related to the projected size R through a power law with approximate index 2, $M \propto R^2$. Observed linewidths for MCs follow a power law relationship with projected size $\sigma \propto R^{1/2}$. Taken together, the interpretation of these relationships is that clouds are (approximately) in virial equilibrium, or “virialized,” so $\sigma^2 \approx GM/R$ (Larson 1981; Dickman et al. 1986; Solomon et al. 1987; Myers & Goodman 1988). Alternatively, if MCs are virialized such that $N_{H_2} \sim M/(\mu R^2) \sim \sigma^2/(\mu GR)$, then $X \sim \sigma^2/(\mu GRW)$. If σ^2/R and W vary little over the population of MCs, then X would have a uniform value.

An open question is whether the “mist” model is applicable to turbulent media, as turbulence is now considered a dominant factor controlling the dynamics of MCs (e.g. Mac Low & Klessen 2004; McKee & Ostriker 2007, and references therein). In the first publication in this series (Shetty et al. 2011, hereafter Paper I), we investigated how well CO can trace the underlying molecular gas using radiative transfer calculations on magnetohydrodynamic (MHD) models of MCs, which include a treatment of chemistry. We focused on velocity integrated CO intensity, and compared probability distribution functions (PDFs) of W , N_{H_2} , and CO column density N_{CO} . We also assessed the X factor, again only considering velocity integrated intensities. We showed that even though X may vary between different LoSs through a given MC, the cloud-averaged intensity

¹ We will hereafter refer to ^{12}CO ($J=1-0$) simply as “CO.”

produces $X \approx X_{\text{Gal}}$ within a factor of 3, from various models with different metallicities $Z/Z_{\odot} = 0.3 - 1$ and densities $n_0 = 100 - 300 \text{ cm}^{-3}$. In this work, we focus primarily on the Milky Way MC model from Paper I, and investigate the properties that affect the derived X factor. Using radiative transfer calculations of turbulent chemo-MHD models, we perform a rigorous theoretical investigation of the qualitative models proposed to explain the observed X factor. We directly modify the cloud characteristics, such as temperature, density, and velocity, and recompute the X factor to understand its dependence on those parameters. Two of our goals are to understand why the X factor is roughly constant for a range of systems, including Milky Way field GMCs, and to assess whether the “mist” model is applicable to turbulent MCs.

This paper is organized as follows. In the next section, we provide an overview of the estimated X factor in various environments. We also discuss the results from Paper I in the context of observationally derived values. In Section 3 we review our method of modeling CO emission from turbulent MCs, and discuss some properties of the main Milky Way MC model. In Section 4, after discussing how the X factor is measured, we compare how X depends on the dynamic, chemical, and thermal structure of the model MC. We investigate in detail the dependence of X on various cloud characteristics, such as temperature, H_2 and CO densities, as well as the velocities. In Section 5 we compare our results to previous observational and theoretical efforts, and offer a new explanation for observed trends. Section 6 summarizes our interpretation of the observed $X \approx X_{\text{Gal}}$ and our conclusions regarding the parameter dependences of X .

2 OVERVIEW OF THE X FACTOR

As alluded to in the previous section, the X factor is found to be nearly constant when considering a specific class of sources, such as Galactic MCs, or a different value for ULIRGs. Yet, analysis of the full spectrum of molecular environments generally portray a trend of decreasing X factor with increasing molecular surface density. Figure 1 shows a compilation of observationally inferred X factors from various systems (Tacconi et al. 2008).

In Paper I, we analyzed the X factor in various models with different metallicities $Z/Z_{\odot} = 0.1 - 1$ and densities $n_0 = 100 - 1000 \text{ cm}^{-3}$. Figure 2 shows the relation between the X factor and surface density Σ_{gas} or N_{H_2} from the various models discussed in Paper I.² The points show the mean X factor averaged in bins of Σ_{gas} , and the large points show the cloud-averaged X factor. At intermediate densities $\Sigma_{\text{gas}} \sim 50 - 200 \text{ M}_{\odot} \text{ pc}^{-2}$, the cloud-averaged X factors for all but the very low $Z=0.1$ model are $\sim 2 - 5 \times 10^{20} \text{ cm}^{-2} \text{ K}^{-1} \text{ km}^{-1} \text{ s} \approx X_{\text{Gal}}$.

Both Figs. 1 and 2 show that X is larger than X_{Gal} in low metallicity systems. As explained in Paper I, large X factor values at low metallicities and densities are primarily due to the low W , the integrated CO intensity, relative to N_{H_2} (Eqn. 1). Systems with lower abundances

of CO will of course have lower W . The formation of CO is highly dependent on the MC density, metallicity, and strength of the background UV radiation field (see also Maloney & Black 1988; van Dishoeck & Black 1988; Glover et al. 2010; Glover & Mac Low 2011). However, H_2 formation is not as sensitive to these properties, due to its ability to effectively self-shield. Thus, the relative abundance of CO compared to H_2 can vary significantly within a MC, leading to a wide range in the X factor, even though the (emission-weighted) average of many different clouds may all result in a value $\sim X_{\text{Gal}}$.

Note that the low surface density regimes in Figs. 1 and 2 are not directly comparable. The low surface densities in our numerical models correspond to diffuse regions in MCs with size $\sim 10 \text{ pc}$. In Figure 1, the low surface density cases correspond to observations with low beam filling factors. These regions can have sizes $\sim \text{kpc}$ (or larger). Therefore, the objects in the two figures may differ in size.

At large surface densities ($\Sigma_{\text{gas}} \gtrsim 200 \text{ M}_{\odot} \text{ pc}^{-2}$), our turbulent models show an increase in the X factor, whereas the observations suggest a decreasing X factor. The increase of X with increasing surface density in our models occurs because in this regime the CO line is saturated, so that W remains constant even as N_{H_2} increases.

Our models only account for the effects of MHD, thermodynamics, and chemical evolution. The sources at high surface densities in Fig. 1 are either the Milky Way center or galaxies undergoing intense star formation activity (LIRGs and ULIRGs). The heating associated with star formation, as well as the large-scale rotation and turbulence of the ISM in these galaxies, are not captured by our models. These processes likely contribute to setting the X factor in such environments, and may be responsible for the observed trends in Figure 1 at high Σ_{gas} .

In our current investigation of the X factor, we aim to understand which MC properties are responsible for $X \sim X_{\text{Gal}}$ in the $50 - 200 \text{ M}_{\odot} \text{ pc}^{-2}$ range. To carry out our analysis, we perform simple experiments by manually changing a number of physical parameters of our models. We then recompute the X factor, and assess which of the modified parameters most affect the resulting value of X .

2.1 Definition of the X factor

We motivate our choice of the parameters to be modified by the definition of the X factor. When the CO intensity is expressed in units of the Rayleigh-Jeans “brightness temperature,” T_B then

$$W = \int T_B dv \text{ (K km s}^{-1}\text{)}. \quad (2)$$

The H_2 column density is simply the volume density integrated over the LoS ds :

$$N_{\text{H}_2} = \int n_{\text{H}_2} ds \quad (3)$$

Taking Equations 1-3 together,

$$X = \frac{\int n_{\text{H}_2} ds}{\int T_B dv}. \quad (4)$$

This indicates that the X factor is explicitly dependent on three quantities: the column density of H_2 , the peak CO

² The conversion between N_{H_2} and Σ_{gas} includes a factor of 1.4 to account for the mass of helium.

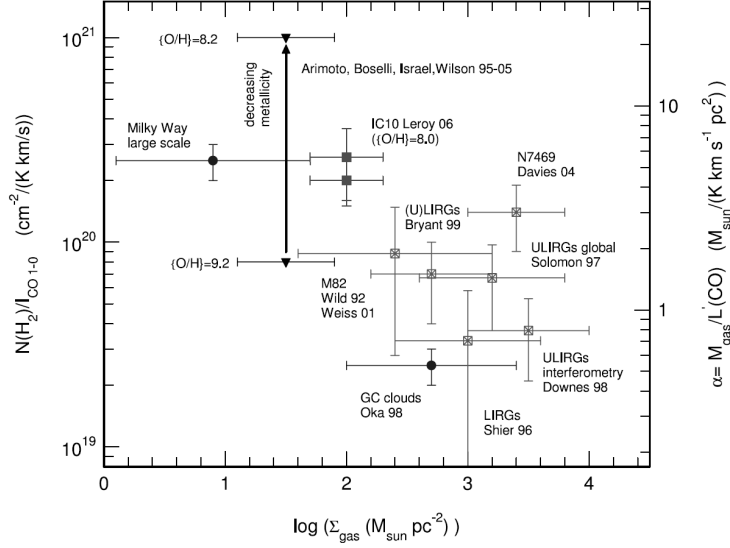


Figure 1. Compilation of estimated X factors from a range of systems, shown as a function of surface density. Figure reproduced from Tacconi et al. (2008).

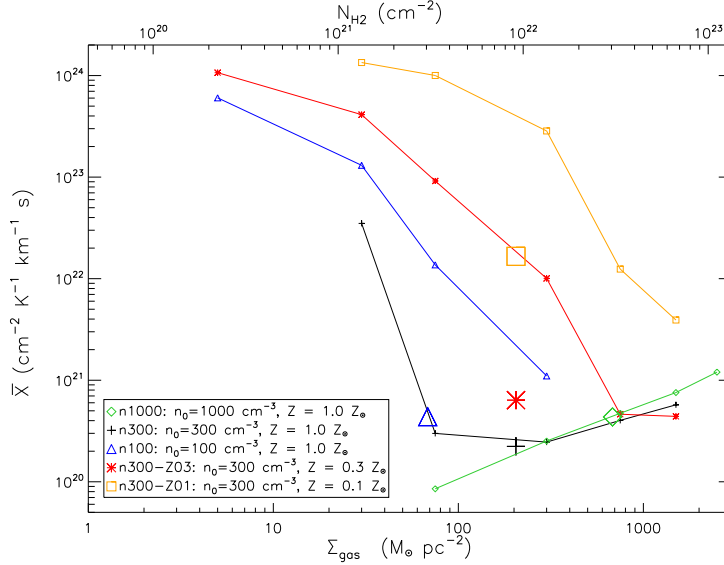


Figure 2. Mean X factor in bins of gas surface density Σ_{gas} (bottom axis) or N_{H_2} (top axis) for 5 models. The X factor is averaged in different Σ_{gas} bins. The value of \bar{X} is plotted on the midpoint value of Σ_{gas} of each bin. Each model is identified by different colors and symbols (and labeled in the legend). The large symbols show the global (emission-weighted) mean X factor and mean Σ_{gas} from each model.

intensity, and the range in velocities. Due to the coupling between hydrodynamics, thermodynamics, and chemistry, T_B is also dependent on the velocity and density (as well as the kinetic temperature). We aim to understand the relative contribution of each of these three properties of the MC. After assessing the X factor from the original Milky Way MC model, we alter one of these properties at a time, while keeping the others fixed, and recompute the X factor. In this manner, we can identify the most important cloud properties responsible for setting the X factor.

3 MODELING METHOD

3.1 Numerical magnetohydrodynamics, chemistry, and radiative transfer

To investigate how MC characteristics affect the X factor, we analyze magnetohydrodynamic (MHD) models of molecular clouds that include a time-dependent treatment of chemistry. We perform radiative transfer calculations on these numerical models, in order to solve for the CO level populations and compute the emergent CO intensity. The ratio of the H_2 column density to the emergent CO intensity then gives the X factor (Eqn. 1).

The MHD grid-based models follow the evolution of an initially fully atomic medium with constant density in

a $(20\text{ pc})^3$ periodic box. Thermodynamics is coupled with chemistry to follow the formation and destruction of 32 chemical species, including H_2 and CO , through 218 chemical reactions. Emission from CO and C^+ are the primary cooling mechanisms in the dense and diffuse regions, respectively. Additionally, a constant background UV radiation field is included, which can photodissociate molecules in regions with insufficient shielding. The photoelectric effect is responsible for most of the heating in the diffuse regions, and in more dense regions heating is primarily due to cosmic ray interactions. Turbulence is driven on large scales (with wavenumbers $1 \leq k \leq 2$) to maintain an approximately constant root mean square (3D) velocity v_{rms} .

For a thorough description of the modeling method, we refer the reader to Glover & Mac Low (2007a,b) and Glover et al. (2010). In this work, we primarily consider the fiducial model chosen to match typical Milky Way MC conditions, which has an initial hydrogen nuclei density $n_0=300\text{ cm}^{-3}$, a metallicity $Z/Z_\odot=1$, a background UV radiation field³ $2.7 \times 10^{-3}\text{ erg cm}^{-2}\text{ s}^{-1}$, and a time averaged turbulent velocity $v_{\text{rms}}=5\text{ km s}^{-1}$. The magnetic field is initially oriented along the \hat{z} -axis, with magnitude $1.95\text{ }\mu\text{G}$.

We use the radiative transfer code RADMC-3D⁴ to calculate the emergent CO intensity. The level populations in each zone are calculated through the Sobolev approximation (Sobolev 1957), which uses velocity gradients across the faces of each grid zone to estimate photon escape probabilities. We employ the Einstein and collisional rate coefficients estimated by Yang et al. (2010) and provided in the LAMDA database (Schöier et al. 2005). A full description of the radiative transfer calculation is provided in Paper I.

The radiative transfer calculations provide the CO intensities at each LoS position (x,y) at a given frequency ν (or velocity) bin, $I_\nu(x,y)$. Besides the viewing geometry and the spectral resolution of the synthetic observation, the only other user defined parameter required to perform the calculation is the microturbulent velocity v_{mtrb} (see Eqns. 2-7 in Paper I). For our fiducial model, we use $v_{\text{mtrb}}=0.5\text{ km s}^{-1}$. In the Appendix, we demonstrate that W or X does not strongly depend on this choice, for $v_{\text{mtrb}} \in 0.25 - 0.75\text{ km s}^{-1}$.

Since we are interested in emission from all the gas in the simulation volume, the spectral channels span the full range in gas velocities. The position-position-velocity (PPV) cube provided by the radiative transfer calculations has a spatial resolution of 0.08 pc or 0.16 pc , corresponding to the extent of the zones in the 256^3 or 128^3 simulations, respectively, and a spectral resolution of 0.06 km s^{-1} .

3.2 The fiducial Milky Way GMC model

Figure 3 shows N_{H_2} and W of the fiducial Milky Way model MC, n300. Though the overall morphology of N_{H_2} is evident in the CO image, there are some stark differences. Most notably, the brightest regions in the CO map (near the bottom) do not correspond to the region with the highest column density (near the top right). This discrepancy

Table 1. Characteristics of Standard “Milky Way GMC” Model (n300)

Property	Value
Box Size L	20.0 pc
Initial Atomic Density n_0	300.0 cm^{-3}
$\langle n_{\text{H}_2} \rangle_{\text{mass}}$	1098.0 cm^{-3}
$\langle n_{\text{H}_2} \rangle_{\text{vol}}$	145.9 cm^{-3}
$\langle T \rangle_{\text{mass}}$	19.8 K
$\langle T \rangle_{\text{vol}}$	51.7 K
$\sigma_{v,\text{los},\text{mass}} = [\langle v_{\text{los}}^2 \rangle_{\text{mass}}]^{\frac{1}{2}}$	2.4 km s^{-1}
$\sigma_{v,\text{los},\text{vol}} = [\langle v_{\text{los}}^2 \rangle_{\text{vol}}]^{\frac{1}{2}}$	2.4 km s^{-1}
$\langle X \rangle_{\text{ref}}$	$1.9 \times 10^{20}\text{ cm}^{-2}\text{ K}^{-1}\text{ km}^{-1}\text{ s}$

arises due to the high optical depth in the CO line. The differences between the observed emission and the underlying gaseous properties of these and other models are described in more detail in Paper I.

Table 1 lists the mass and volume weighted H_2 number densities, temperatures, and LoS rms velocities⁵ $\langle v_{\text{los}}^2 \rangle^{1/2} = \sigma_{v,\text{los}}$, along with the initial density n_0 and box size L of model n300. Mass and volume weighted quantities are defined as $\langle f \rangle_{\text{mass}} = \sum f \rho dV / \sum \rho dV$ and $\langle f \rangle_{\text{vol}} = \sum f dV / \sum dV$, respectively.⁶ The last row of Table 1 shows a reference value of the X factor: $\langle X \rangle_{\text{ref}} \equiv \langle n_{\text{H}_2} \rangle_{\text{vol}} L / [\langle T \rangle_{\text{mass}} \sigma_{v,\text{los}}]$.

As discussed in Paper I and Glover et al. (2010), the internal properties of the fiducial Milky Way cloud model take on a range on values. For example the CO abundance relative to H_2 , f_{CO} , can vary from $\sim 10^{-9}$ to 10^{-4} . Similarly, the temperature, density, and velocity also take on a wide range of values. Throughout our analysis, besides considering CO emission from the original model, we also consider models for which some relevant physical characteristics are modified, such as those with constant temperature or CO abundances. In this manner, we can quantitatively assess the effect of the various physical characteristics on the emergent CO intensity, and ultimately on the X factor.

4 RESULTS

4.1 Measuring the X factor

We begin by calculating the X factor through its traditional definition given by Equation 1. Figure 4 shows the mean X factor in bins of N_{H_2} as a function of N_{H_2} from all LoSs through the fiducial model⁷. As explained in Paper I, at the highest densities W does not increase with increasing N_{H_2}

⁵ Since the viewing angle is along the \hat{z} -axis, $v_{\text{los}} = v_z$. Due to large-scale stochastic variations, the dispersion in v_z is not exactly equal to $v_{\text{rms}}/\sqrt{3}$.

⁶ $\langle n_{\text{H}_2} \rangle_{\text{vol}}$ is not exactly 150 cm^{-3} because a small fraction of hydrogen remains atomic (Glover & Mac Low 2011).

⁷ Though the figures presented here only show the results from one viewing angle (along the \hat{z} -axis) we have verified that the results are not sensitive to any chosen viewing direction.

³ This value is $1.7G_0$ as determined by Draine (1978), where G_0 is the Habing (1968) field.

⁴ www.ita.uni-heidelberg.de/~dullemond/software/radmc-3d/

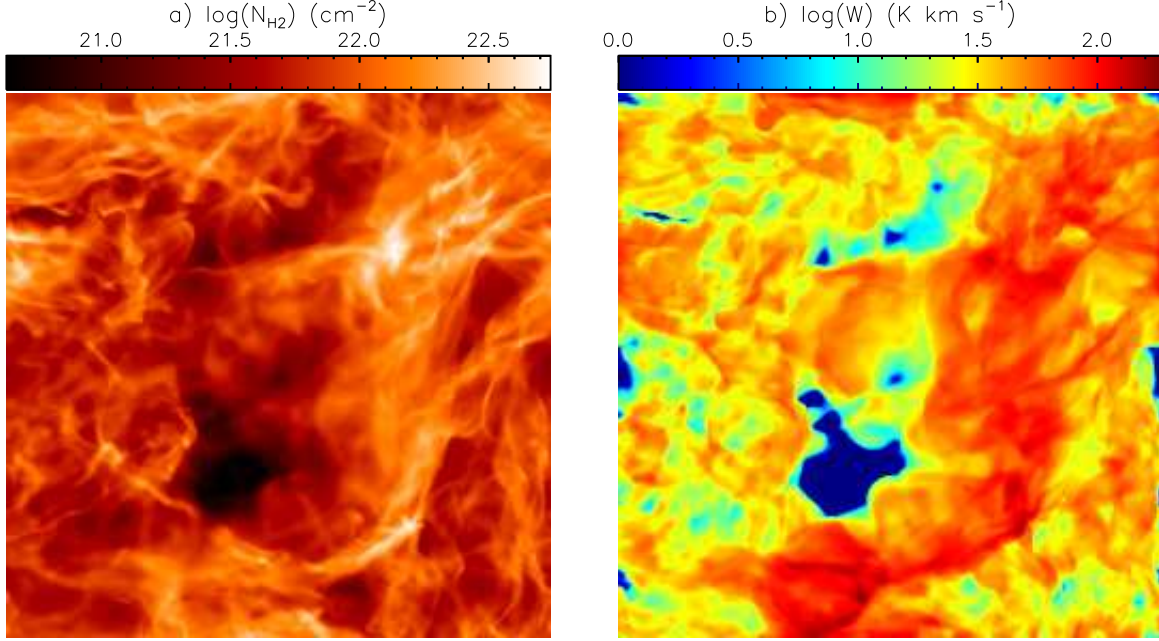


Figure 3. a) Column density N_{H_2} and b) integrated CO intensity of the Milky Way model MC.

due to the saturation of the CO line, resulting in $X \propto N_{\text{H}_2}$. Nevertheless, the mean X factor only varies between $(1.5 - 4) \times 10^{20} \text{ cm}^{-2} \text{ K}^{-1} \text{ km}^{-1} \text{ s}$ for $\log N_{\text{H}_2} = 21-22.5$. Given this limited range and the extent of the error bars, a constant value at its emission-weighted mean value⁸ (shown by the large filled circle in Fig. [4]) adequately describes the X factor for this model. This mean X factor value $\langle X \rangle = 2.2 \times 10^{20}$ is in good agreement with the reference value provided in Table 1, $\langle X \rangle = 1.9 \times 10^{20}$. We now consider the terms N_{H_2} and W in detail, and their relationship to the physical properties of the model.

Instead of integrating Equation 3 over the whole cloud, one could only use a limited range in velocity (or frequency, ν).

$$N_{\text{H}_2, \nu} = \int n_{\text{H}_2} dv. \quad (5)$$

If $N_{\text{H}_2, \nu}$ is computed along the same LoS and in velocity bins that match the spectral channels of the CO observation, then a column density cube of $N_{\text{H}_2, \nu}$ can be constructed which has the same configuration as the observed CO position-position-velocity (PPV) cube.

We can now define the X factor at each PPV location, X_ν , associated with column density $N_{\text{H}_2, \nu}$, intensity T_B and adopted channel width Δv (in our case, 0.06 km s^{-1}):

$$X_\nu = \frac{N_{\text{H}_2, \nu}}{T_B \Delta v}. \quad (6)$$

Figure 5 shows how this “3D X factor” depends on the column density for the Milky Way model cloud. Here, $N_{\text{H}_2, \nu}$ extends to much lower values than the values of N_{H_2} shown

in Figure 4, since the volume densities are integrated over a more limited region (in velocity space).

The emission weighted mean “3D X factor” is equal to X factor computed in its usual way, shown in Figure 4. However, at high densities, X_ν is significantly larger than X , reaching values $\gtrsim 10^{22} \text{ cm}^{-2} \text{ K}^{-1} \text{ km}^{-1} \text{ s}$, whereas the 2D X factor is always $\lesssim 10^{21} \text{ cm}^{-2} \text{ K}^{-1} \text{ km}^{-1} \text{ s}$. From Figure 5, it is clear that the CO line is saturated at column densities (per frequency bin) above the mean column density $\overline{N_{\text{H}_2, \nu}} = 3.5 \times 10^{19} \text{ cm}^{-2}$, as indicated by the $N_{\text{H}_2, \nu} / (\overline{T_B} \Delta v)$ line, where $\overline{T_B}$ is the mean brightness temperature in PPV regions where $N_{\text{H}_2, \nu} > \overline{N_{\text{H}_2, \nu}}$.

The discrepancy at high column densities between X and X_ν is due entirely to the differences between W and $T_B \Delta v$. On a given LoS, W is the summation of $T_B \Delta v$ through all velocities in the PPV cube. Figure 6 shows these quantities as a function of N_{H_2} or $N_{\text{H}_2, \nu}$, respectively. Clearly, W continues to increase beyond $N_{\text{H}_2} \gtrsim 10^{21} \text{ cm}^{-2}$, whereas $T_B \Delta v$ is saturated. Since Δv is constant, this means that T_B saturates at a value $\sim 13 \text{ K}$.⁹

Line saturation occurs when the optical depth at a given frequency ν , $\tau_\nu \gtrsim 1$. The optical depth along a LoS of length s is given by

$$\tau_\nu = \int \frac{h\nu}{4\pi} (n_1 B_{12} - n_2 B_{21}) \phi_\nu ds, \quad (7)$$

where h , n_i , and B_{ij} are the Planck constant, population number density in level i , and the Einstein (stimulated absorption/emission) coefficients. The normalized line profile function ϕ_ν depends on the LoS and microturbulent veloci-

⁸ We denote any weighted-mean value with $\langle \dots \rangle$, whereas simple averages with an “overline” (e.g. \overline{W}).

⁹ This saturation brightness temperature is estimated from Figure 6, which shows the mean values of $T_B \Delta v$ in bins of $N_{\text{H}_2, \nu}$. The maximum T_B can reach values $\gtrsim 30 \text{ K}$.

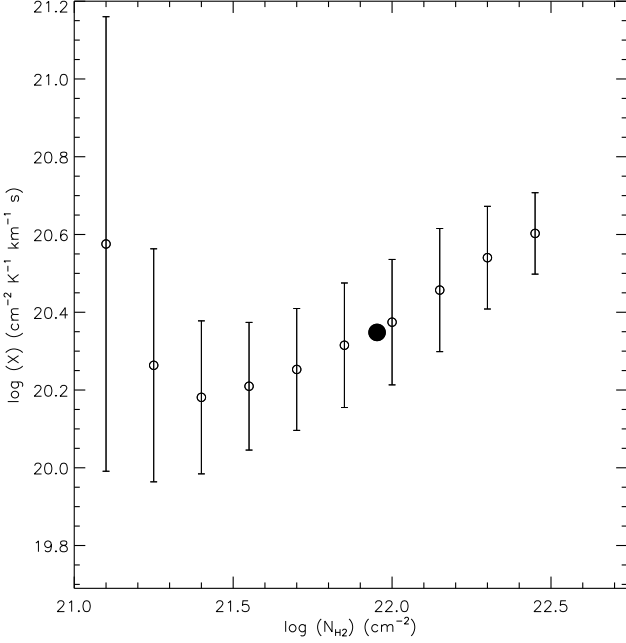


Figure 4. X factor from the Milky Way model molecular cloud. The open circles and error bars indicate the mean and standard deviation of the X factor in bins of N_{H_2} . The solid circle shows emission weighted mean X factor of the whole model ($\langle X \rangle = 2.2 \times 10^{20} \text{ cm}^{-2} \text{ K}^{-1} \text{ km}^{-1} \text{ s}$) at the mean column density ($\overline{N_{\text{H}_2}} = 9.0 \times 10^{21} \text{ cm}^{-2}$, corresponding to $\overline{\Sigma_{\text{gas}}} = 202 \text{ M}_{\odot} \text{ pc}^{-2}$).

ties, as well as the kinetic temperature (see Section 2.2 of Paper I for more details). Together, the density, temperature, and velocity structure of the molecular cloud determines the optical depth, and therefore where the line is saturated.

The mean and minimum value of τ_{ν} , in bins of $N_{\text{H}_2, \nu}$, are also shown in Figure 6, with the scale given on the right ordinate. Though $T_B \Delta v$ does not vary much in the range of the high column densities shown in Figure 6, a trend of increasing $T_B \Delta v$ with column density is apparent until the $N_{\text{H}_2, \nu} \approx 10^{20.5} \text{ cm}^{-2}$. At column densities $N_{\text{H}_2, \nu} \approx 10^{21} \text{ cm}^{-2}$, all values of $\tau_{\nu} > 1$, indicating complete saturation of $T_B \Delta v$.

That the velocity-integrated brightness temperature W still increases beyond $N_{\text{H}_2} \gtrsim 10^{20.5} \text{ cm}^{-2}$, where the line is saturated, indicates that numerous optically thick regions at different v contribute to W . This results in the saturation of the integrated intensities occurring at higher column densities than the saturation of the intensities in the PPV cube, as evident at the highest N_{H_2} in Figure 6.

One consequence of the line saturation described above is that the amount of gas that is untraced depends not only on the density, but also on the velocity. For instance, a “cloudlet” or parcel of dense gas with similar velocity as another parcel along a LoS, but separated in space, would not contribute extra flux to T_B , or the W map. On the other hand, a “cloudlet” with much different velocity along the LoS would be traced, detected as higher T_B at a different location in the velocity axis of the spectrum, and thus contribute to the integrated intensity W . Consequently, LoSs with (dense) gas spanning a larger range in velocities

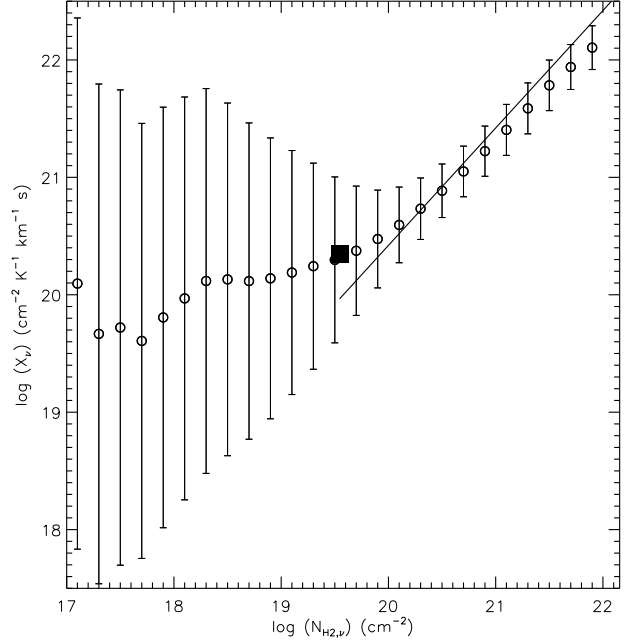


Figure 5. X_{ν} vs. $N_{\text{H}_2, \nu}$ from the Milky Way model molecular cloud. The mean and standard deviation of X_{ν} in bins of $N_{\text{H}_2, \nu}$ are shown as circles with error bars. The solid square shows emission weighted mean X_{ν} of the whole model ($\langle X_{\nu} \rangle = 2.2 \times 10^{20} \text{ cm}^{-2} \text{ K}^{-1} \text{ km}^{-1} \text{ s}$) at the mean column density ($\overline{N_{\text{H}_2, \nu}} = 3.5 \times 10^{19} \text{ cm}^{-2}$). Line shows $N_{\text{H}_2, \nu} / (T_B \Delta v)$ at $N_{\text{H}_2, \nu} > \overline{N_{\text{H}_2, \nu}}$.

will have larger W s. This concept of optically thick dense “cloudlets” is the basis of the “mist” model put forth by Solomon et al. (1987) to explain the uniformity in the X factor in Galactic GMCs. We return to the applicability of the “mist” model in Section 4.5.

The differences in the relationships between W and $T_B \Delta v$ with column density (Fig. 6) lead to the variations between X and X_{ν} (Figs. 4 and 5). The (2D) X and (3D) X_{ν} distributions are shown in Figure 7. Though the peak value of the two distributions are similar, there is a much larger distribution in X_{ν} . In considering synthetic observations with different spectral resolution, we find that the range in X_{ν} depends on Δv , but that $\langle X_{\nu} \rangle = 2.2 \times 10^{20} \text{ cm}^{-2} \text{ K}^{-1} \text{ km}^{-1} \text{ s}$ consistently. As discussed, there are lower column densities $N_{\text{H}_2, \nu}$ in a PPV cube compared to N_{H_2} . For such densities, the line is often optically thin, and there is a range of possible emergent intensities for a given column density (Fig. 6). This results in a larger range in X_{ν} compared to X .

Taken together, the limited range in the 2D X factor shown in Figure 4 and 7 only occurs when the CO intensities are integrated over all velocities, and densities over the whole LoS. Effectively, a limited range in the X factor only results when combining the detailed velocity, as well as density, structure along the LoS. This is indicative that the velocity range plays a crucial role in setting the X factor.

Of course, integrating the observed brightness temperatures over a limited range in velocity is not practical, as obtaining $N_{\text{H}_2, \nu}$ is not readily feasible in observational data sets. Nevertheless, such an analysis has underscored that the X factor depends on the total velocity width of the cloud, as

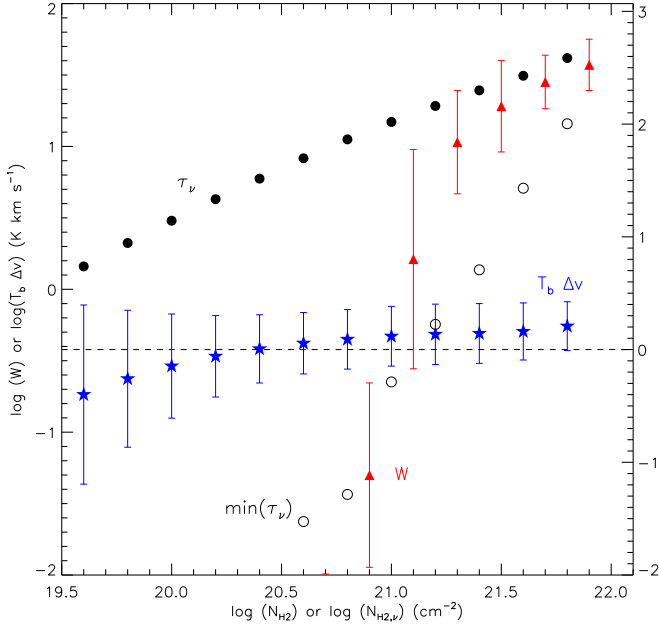


Figure 6. Intensity (left ordinate) and optical depth (right ordinate) plotted against column densities. Triangles show the mean integrated CO intensity W as a function of total column density $N_{\text{H}_2}(2\text{D})$. Stars show the analogous relationship from (3D) PPV cubes, $T_B \Delta v$ vs $N_{\text{H}_2,\nu}$. Filled circles show the mean optical depth τ_ν , and the open circles show the minimum value of τ_ν in the $N_{\text{H}_2,\nu}$ bins. Dashed line corresponds to $\tau_\nu=1$.

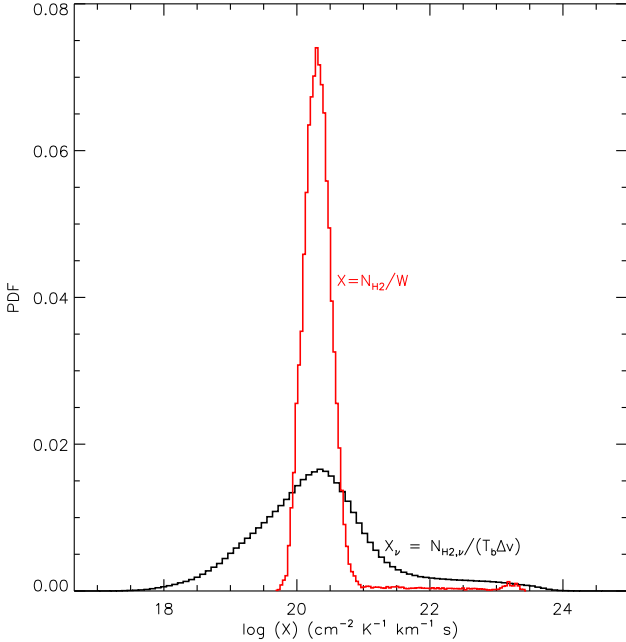


Figure 7. PDFs of X factors shown in Figures 4 and 5.

explicitly evident in Equation 4. But, how does the detailed velocity structure, such as its relationship with the size of emitting regions, affect the X factor? Further, what is the relative contribution of $\int dv$ compared to the other terms n_{H_2} and T_B in Equation 4? To address these questions, we investigate in detail the role of each quantity in determining the nature of the CO emission, and their relationship to intrinsic cloud properties.

4.2 X factor dependence on temperature

Due to the thermodynamics in the chemical-MHD model, the gas has a range of temperatures. As indicated in Table 1, the model MC has a (volume-weighted) mean $T \approx 50$ K, with a dispersion $\sigma \approx 44$ K. This range in temperatures will also result in a range in the X factor, since the observed brightness temperature depends on the gas kinetic temperature (Eqn. 2).

To test the sensitivity of the X factor to the temperature distribution, we artificially set all temperatures in the model to a constant value, and then perform the radiative transfer calculations. The resulting maps are then compared with the original CO map. Any discrepancies can be attributed to the differences in temperatures.

This is illustrated in Figure 8, where (a) shows the original distribution of X , and (b) - (d) show the X factors for constant temperatures of 25, 50, and 100 K. The histograms from the model with the original temperatures are provided in each panel as dashed lines.

The constant temperature $T = 20$ K model, equal to the mass-weighted temperature (see Table 1), provides an X factor distribution that is very similar to the original model (Figs. 8b). This is expected since most of the CO is located in dense regions where $T \lesssim 20$ K. The relationship between X , N_{H_2} , and N_{CO} is also rather comparable to the original relationship. Note that for both the original and constant $T=20$ K models, the highest and lowest values of N_{H_2} have large X . (cf. Fig. 4). The differences between the 20 K and 50 K model suggests that the X factor is more sensitive to the mass-weighted rather than the volume-weighted temperatures.

Figure 9 shows the mean X in bins of N_{H_2} from the original model (as in Fig. 4), along with two reference values obtained directly from the simulation. The red stars show X computed using the mass-weighted LoS velocity and global mass-weighted temperature. The blue triangles show the corresponding X from the volume-weighted quantities. Along LoSs with column densities lower than $\lesssim 10^{21.8} \text{ cm}^{-2}$, the CO fraction decreases, thereby decreasing W (see Paper I and Section 4.3.2). Thus, the simple relationships between X , T , and v_{los} cannot reproduce the X factor at low column densities. At column densities $\gtrsim 10^{21.8} \text{ cm}^{-2}$, however, the X factor computed using the mass-weighted temperature agrees fairly well with the original X factor. The X factor computed from the volume-weighted temperature systematically underestimates the X factor. These trends indicate that the densest regions contribute most to setting W , and thereby the X factor.

As indicated in Figure 8, clouds with higher temperatures produce lower X factors, as would expected from Eqn. 1-2. From $\langle X \rangle = 1.8 \times 10^{20}$, 1.1×10^{20} , and $7.9 \times 10^{19} \text{ cm}^{-2} \text{ K}^{-1} \text{ km}^{-1} \text{ s}$ at $T = 20, 50$, and 100 K, respectively, we find

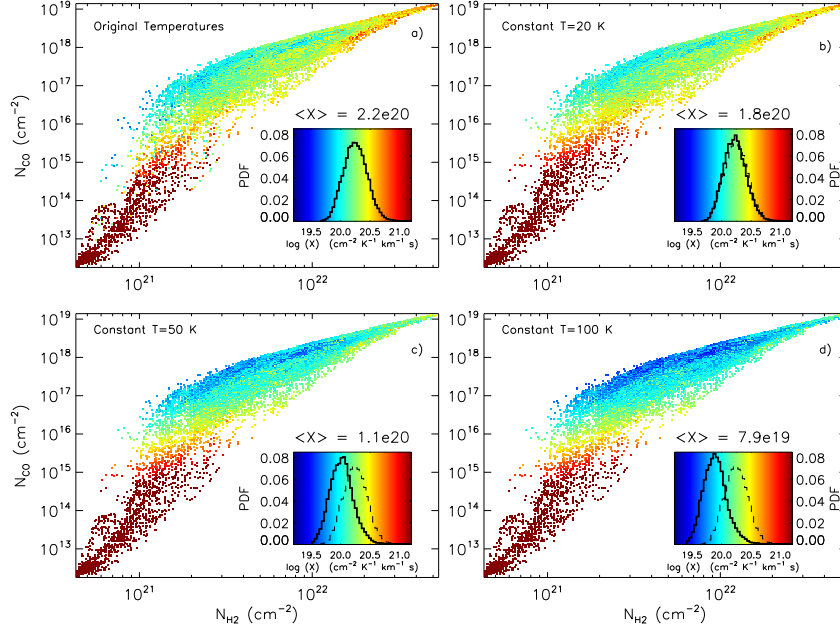


Figure 8. The variation of the X factor with gas temperature. The position of each point shows the relationship between N_{H_2} and N_{CO} . The color of each point identifies the value of the X factor, computed through Eqn. 1, with the color scale and distribution given in the inset plots. The emission-weighted mean value $\langle X \rangle$ is indicated in each plot. a) Original model n300, b) model n300, but with constant $T=20$ K, c) constant $T=50$ K, and d) constant $T=100$. In b), c), and d), X factor distribution from original simulation in a) is shown as thin dashed histogram.

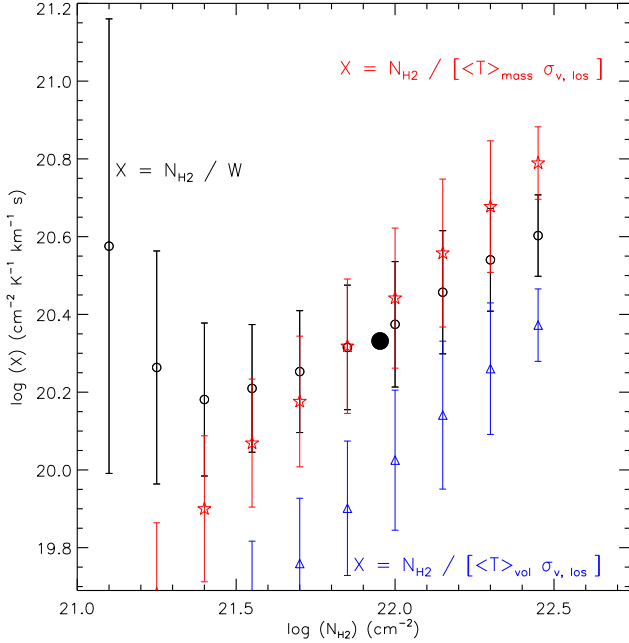


Figure 9. X factor (black circles) from the Milky Way model molecular cloud, as in Fig. 4. The emission-weighted mean X at the mean column density is shown by the large solid circle. Red stars show the the X factor computed by $N_{\text{H}_2}/\langle T \rangle_{\text{mass}} \sigma_{v,\text{los}}$, and blue triangles show $N_{\text{H}_2}/\langle T \rangle_{\text{vol}} \sigma_{v,\text{los}}$. $\langle T \rangle_{\text{mass}}$ and $\langle T \rangle_{\text{vol}}$ are the global mass-weighted and volume-weighted temperatures, given in Table 1. $\sigma_{v,\text{los}}$ is the mass-weighted rms velocity (which is equal to the volume-weighted rms velocity) along each LoS.

an approximate scaling $\langle X \rangle \propto T^{-0.5}$. The range in the X factors in the modified-temperature models is, however, similar to the original model. This indicates that the range in temperatures in model n300 is not responsible for the range in the X factor. As a result, it is either the range in densities or the velocities which produce the distribution in the X factor.

We note that an increase in temperature to 100 K is likely accompanied by other variations in the molecular cloud structure, such as a decrease in n_{H_2} and possibly f_{CO} if the high temperature is due to a high star formation rate. As such, models for which the temperatures are manually scaled to high values are likely omitting real environmental effects that would affect the X - T relationship.

4.3 X factor dependence on density

We turn our attention to the X factor dependence on density. Any given cloud will have a range in volume and column densities, in both H_2 and CO . If W depends linearly on N_{H_2} , then there would certainly be a constant X factor along all LoSs. However, as discussed in Paper I, W generally does not have a straightforward scaling with the column density N_{CO} , especially at large N_{CO} due to the high opacity of CO (see Section 4.1). Further, N_{CO} does not directly trace N_{H_2} . This lack of correlation between W and N_{H_2} results in a distribution of X along different LoSs for a given MC. We focus on how the volume density and CO abundance affect the X factor.

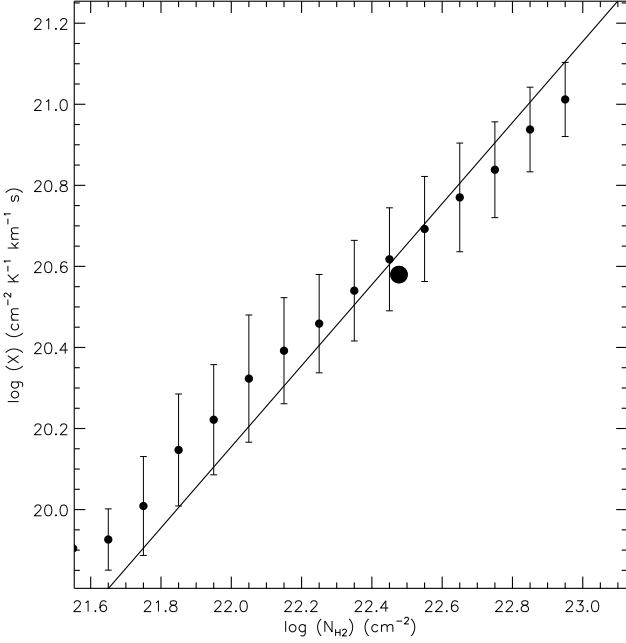


Figure 10. X factor vs. N_{H_2} from model n1000, which has box size $(20 \text{ pc})^3$. The line shows $X = N_{\text{H}_2}/\overline{W}$, with $\overline{W} = 70 \text{ K km s}^{-1}$. The large circle shows $\langle X \rangle = 3.8 \times 10^{20} \text{ cm}^{-2} \text{ K}^{-1} \text{ km}^{-1} \text{ s}$ at $\overline{N}_{\text{H}_2} = 3.0 \times 10^{22} \text{ cm}^{-2}$, or $\overline{\Sigma}_{\text{gas}} = 672 \text{ M}_{\odot} \text{ pc}^{-2}$.

4.3.1 X factor dependence on volume density

To test whether the X factor is more sensitive to n_{H_2} or to N_{H_2} , we consider a model with a higher volume density than model n300. This model (n1000), only differs from model n300 in its initial atomic density of 1000 cm^{-3} . As described in Paper I, most of the carbon in this model is incorporated into CO, and so there is a very good correlation between N_{CO} and N_{H_2} (see Fig. 5c in Paper I).

As explained in Paper I, for this high density model the effect of line saturation is clearly apparent in the X factor computed through Equation 1. Figure 10 shows the relationship between X and N_{H_2} for model n1000. The line is not a fit, but rather the relationship $X = N_{\text{H}_2}/\overline{W}$, where $\overline{W} = 67 \text{ K km s}^{-1}$ is the mean integrated intensity from this model. We see that X invariably increases with N_{H_2} , as would be expected if the line were saturated.

The X – N_{H_2} relationship for model n300 (Fig. 4) is quite different from the relationship from model n1000, due partly to the larger maximum column density in model n1000 and lower minimum column density in model n300. We investigate whether the total column density, which occurs explicitly in Equation 1 is responsible for the increase in X at large N_{H_2} in model n1000. We perform the radiative transfer calculations on a model which is similar to n1000, but whose box length is decreased by a factor of ~ 3 to 6 pc. In this n1000-L6 model, the lower column densities allow the background UV radiation to penetrate further into the cloud, leading to more CO photodissociation. Nevertheless, this model should have similar H_2 column densities to the n300 model, since H_2 can self-shield more efficiently. On the other hand, the volume densities in n1000-L6 will be very similar to those in the n1000 model.

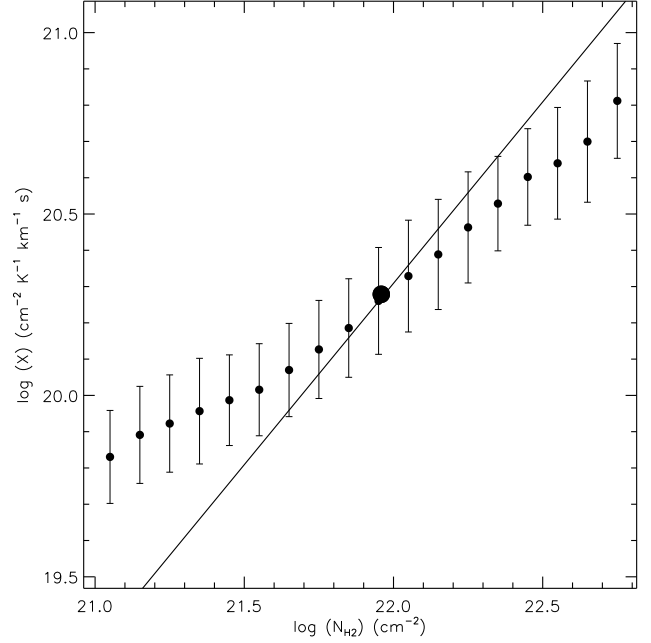


Figure 11. X factor vs. N_{H_2} from model n1000-L6, which has initial density 1000 cm^{-3} and box size $(6 \text{ pc})^3$. Line shows $X = N_{\text{H}_2}/\overline{W}$, with $\overline{W} = 49 \text{ K km s}^{-1}$. The large circle shows $\langle X \rangle = 1.9 \times 10^{20} \text{ cm}^{-2} \text{ K}^{-1} \text{ km}^{-1} \text{ s}$ at $\overline{N}_{\text{H}_2} = 9.1 \times 10^{21} \text{ cm}^{-2}$ corresponding to $\overline{\Sigma}_{\text{gas}} = 204 \text{ M}_{\odot} \text{ pc}^{-2}$.

Figure 11 shows the X – N_{H_2} relation for this n1000-L6 model. The line shows $X = N_{\text{H}_2}/\overline{W}$, with $\overline{W} = 49 \text{ K km s}^{-1}$ for this model. Here, $\langle X \rangle$ is similar to the n300 model. The X – N_{H_2} relation is not as well reproduced by the $N_{\text{H}_2}/\overline{W}$ line as model n1000 in Figure 10. Nevertheless, the X factor clearly increases with N_{H_2} . Compared to model n300 (Fig. 4), X is similar for $N_{\text{H}_2} \sim 10^{22} - 10^{22.5} \text{ cm}^{-2}$, but there are significant differences at lower N_{H_2} , especially $\lesssim 10^{21.5}$. Thus, *the X factor, even when calculated using the total column density (Eqn. 1), depends on the volume density n_{H_2} , rather than just the column density N_{H_2} .* Note, however, that when averaged over all lines of sight, $\langle X \rangle$ decreases by only 15% even though n_0 increases by a factor 3.3.

4.3.2 X factor dependence on CO abundance

Besides containing a range in densities, there is also a range in CO abundances at a given H_2 density, as is evident in the column density relationships in Fig. 8 (see also Paper I, and Glover et al. 2010). In order to investigate how this distribution contributes to the X factor, we reset the CO abundance with a constant $f_{\text{CO}} = n_{\text{CO}}/n_{\text{H}_2}$ ratio, and then perform the radiative transfer calculations.

Figure 12 shows the X factor – N_{H_2} relation for (a) the original model, as well as those with (b) constant $f_{\text{CO}} = 10^{-4}$, (c) 10^{-5} , and (d) 10^{-6} . Also shown in each panel is the line corresponding to the $X = N_{\text{H}_2}/\overline{W}$ relation, indicating complete saturation of the CO line.

With the original abundances, the $X = N_{\text{H}_2}/\overline{W}$ relationship is close to the model values only at the highest column densities. At densities $\lesssim 3 \times 10^{21} \text{ cm}^{-2}$, the over-

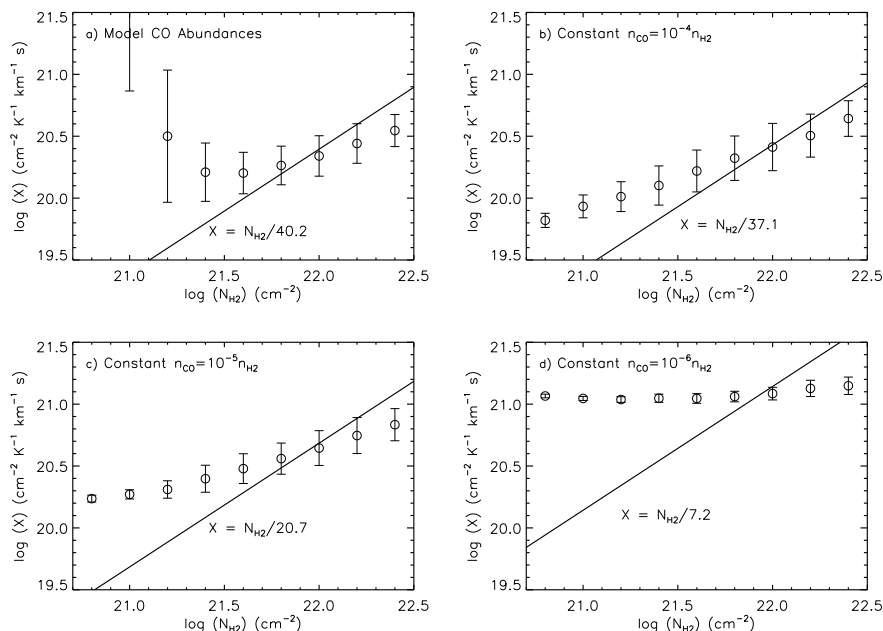


Figure 12. The X factor– N_{H_2} relationship from model n300, as in Figure 4 (a), but with the CO number density reset to be (b) 10^{-4} , (c) 10^{-5} , and (d) $10^{-6} \times n_{\text{H}_2}$. Line in each plot shows $X = N_{\text{H}_2}/\bar{W}$ relation.

plotted line underestimates X . In this regime, CO emission is not saturated. Figure 12b is analogous to the limiting scenario where all the atomic carbon and oxygen is converted to CO, so that $f_{\text{CO}}=10^{-4}$. For this model, the $X = N_{\text{H}_2}/\bar{W}$ relation is similar to the data above $N_{\text{H}_2} \sim 10^{21.5} \text{ cm}^{-2}$, indicating that the CO line is nearly fully saturated. In Figure 12c-d, with lower f_{CO} , line saturation becomes less and less important, especially at lower column densities, finally resulting in a constant X and N_{H_2} relation for $f_{\text{CO}}=10^{-6}$.

In general, the CO line becomes saturated in regions with the highest CO abundance. With constant $f_{\text{CO}}=10^{-4}$, X increases with increasing N_{H_2} everywhere, and the CO line is completely saturated at column densities $\gtrsim 10^{21.5} \text{ cm}^{-2}$ (Fig. 12b), resulting $X \propto N_{\text{H}_2}$. At lower CO abundances, W increases with increasing column density. This results in a shallower slope in the $X - N_{\text{H}_2}$ relation. At very low $f_{\text{CO}}=10^{-6}$, W is directly proportional to N_{H_2} , so that X is constant at all N_{H_2} . Taken together, clouds with both low and high CO abundances will tend to have a more limited range in X than a cloud with only large f_{CO} , which would have $X \propto N_{\text{H}_2}$.

Notice that in Figure 12d, $X=10^{21} \text{ cm}^{-2} \text{ K}^{-1} \text{ km}^{-1}$ s, for the model with CO abundance $f_{\text{CO}}=10^{-6}$. This is the quoted abundance in diffuse Milky Way gas observed by Burgh et al. (2007) and Liszt et al. (2010). However, Liszt et al. (2010) find $X \approx 3 \times 10^{20} \approx X_{\text{Gal}}$, which is a factor ~ 5 lower than the resulting value in Fig. 12d. The discrepancy is likely due to the combination of the differences in temperature and linewidths between the “diffuse” MCs and more massive giant MCs. The diffuse ISM has a higher temperature, up to $\sim 100 \text{ K}$. As we demonstrate in Section 4.2, such high temperatures may account for a significant fraction of the difference. Further, observations of low column density LoSs probably trace a larger volume of

the Galaxy, thereby including gas with a wider range in velocities than those found in MCs. As we discuss in the next section, larger velocities may lead to lower X factor values. Nevertheless, note that the discrepancy may be partly due to the fact that in this numerical experiment, we artificially fix the CO abundance. The metallicity and self-shielding are not self-consistently tracked in these experiments.

4.4 X factor dependence on velocity

In order to test the sensitivity of the X factor to the velocity v_{los} or the integral over dv appearing in Equation 4, we consider MC models with different velocity fields. In the MHD simulations, turbulence is generated by continuously driving the gas velocities with uniform power between wavenumbers $1 \leq k \leq 2$. In the standard Milky Way MC model presented so far, the saturation amplitude of the 1D velocity dispersion is 2.4 km s^{-1} .

We test the effect of velocities by performing experiments on two different sets of models for which the velocities differ from the fiducial n300 model. The first set of models have different driven turbulent velocities. In these experiments, the other parameters of the simulations are identical to that from model n300 - only the saturated-state (3D rms) velocities differ by factors of 0.2 and 2. The second set of models are simply the original n300 models, but for which the velocities in each zone are manually modified. As discussed in Paper I, the chemical evolution is not strongly affected by the velocity field. It is the metallicity, density, and background UV radiation field which are the primary factors determining CO formation (see also Glover et al. 2010; Glover & Mac Low 2011). Given the insensitivity of molecule formation to the velocity field, we can directly modify the velocities in model n300. We thus con-

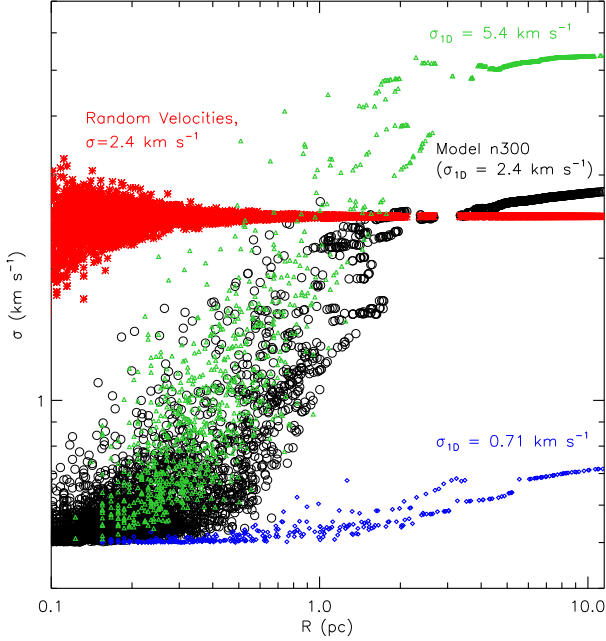


Figure 13. The linewidth-size relationship from model n300. Structures are identified directly from the 3D simulation. The linewidths σ are computed by taking the dispersion of the (1D, or v_z) velocities from the identified structures in the simulations (black, blue, and green) or from a Gaussian distribution with a dispersion of 2.4 km s^{-1} (red).

sider models with chosen velocity dispersions, where all the other parameters are equivalent to those in model n300.

4.4.1 Different levels of turbulence

Figure 13 shows the linewidth-size relations for clumps in the MHD models. “Clumps” are identified directly from the simulation (in the 3D density cube), through dendrograms (Rosolowsky et al. 2008). The dendrogram¹⁰ algorithm identifies contiguous structures through iso-density contours. The linewidth of each clump is computed from the dispersion in the corresponding region from the 3D v_z -cube.¹¹ As evident in Figure 13, the linewidth-size relationship can be reasonably expressed as a power law $\sigma \propto R^a$. For the original n300 model (black circles) the best fit exponent $a=0.45$. This is in good agreement to the observed linewidth size relationship (e.g. Larson 1981; Solomon et al. 1987; Heyer et al. 2009). At small radii approaching the resolution limit of the simulation, the velocities approach a minimum threshold corresponding to the microturbulent velocity of 0.5 km s^{-1} . This chosen value of the microturbulent velocity is greater than the thermal velocity due to the observed linewidths at $\sim 0.1 \text{ pc}$ scales. At large scales, the 1D linewidths $\sim 2.4 \text{ km s}^{-1}$ are the overall dispersion in the LoS velocities.

The blue and green points in Figure 13 show the σ -

R relationship from simulations with different forcing amplitudes, with 3D $v_{\text{rms}} \approx 1$ and 10 km s^{-1} , producing LoS velocity dispersions of 0.71 and 5.8 km s^{-1} , respectively.¹² For these simulations, the best fit power laws produce $a = 0.08$ and 0.61 , respectively. The red points in Figure 13 show the linewidth-size relationship from a model similar to n300, but with the velocities drawn from a random distribution with $\sigma = 2.4 \text{ km s}^{-1}$ (which produces $a=0$).

Figure 14 shows the relationship between X , N_{H_2} , and N_{CO} from the original n300 model, along with the models with different velocity fields. In Figure 14b - f, the velocities vary due to a different turbulent forcing amplitude, or simply due to replacing the velocities from the n300 MHD simulation with a Gaussian distribution. As discussed, the original velocities in model n300, (Fig. 14a) have a LoS dispersion of $\sigma = 2.4 \text{ km s}^{-1}$, due to turbulent forcing with 3D (rms) mean dispersion $v_{\text{rms}} = 5 \text{ km s}^{-1}$.

Figure 14(c) and (e) show the X factor from models where the turbulent forcing is varied from the original n300 to yield $\sigma_{1D} \approx 0.71 \text{ km s}^{-1}$, or $\sigma_{1D} \approx 5.8 \text{ km s}^{-1}$, respectively. Figure 13 demonstrates that the velocities of the large scale structures in these model vary by a factor of ~ 3 above and below the original n300 model, but are rather similar on the smallest scales due to the imposed microturbulence. Because the turbulent driving varies, the gas in these models contain different amounts of CO, and different temperatures. Comparing the other properties of these models (in Table 1), the lower velocities in the 0.71 km s^{-1} model result in lower temperatures ($\langle T \rangle_{\text{vol}} = 24 \text{ K}$), and lower amounts of total CO (as well as H_2 , $\langle n_{\text{H}_2} \rangle_{\text{vol}} = 127 \text{ cm}^{-3}$). The 5.8 km s^{-1} model, on the other hand, has $\langle T \rangle_{\text{mass}} = 27 \text{ K}$. Nevertheless, the X factor for these models are both within $\sim 50\%$ of the n300 value ($\langle X \rangle = 3.4 \times 10^{20}$, 2.2×10^{20} , and $1.6 \times 10^{20} \text{ cm}^{-2} \text{ K}^{-1} \text{ km}^{-1} \text{ s}$, respectively, for $\sigma_{1D} = 0.71 \text{ km s}^{-1}$, 2.4 km s^{-1} , and 5.8 km s^{-1}).

4.4.2 Purely Gaussian Velocities

The right panels in Figure 14 shows the X factor from model n300, but with the velocities replaced with random values drawn from a Gaussian distribution with $\sigma =$ b) 2.4 , d) 24 , and e) 240 km s^{-1} . For the $\sigma = 2.4 \text{ km s}^{-1}$ model, the linewidth-size relationship differs significantly (Fig. 13) from the fiducial model n300. The dispersions are similar on large scales, by design. However, at smaller scales the dispersions in the original model decreases, whereas there is a constant dispersion on all scales in the modified model. Nevertheless, the X factor distribution is very similar to the original model n300. The globally averaged X factor from the original model is recovered. That the X factor is very similar to the original model suggests that *the details of the velocity structure, and its relationship to other physical properties such as mass or size, do not play an important role in determining the X factor*. In particular, clouds with very different linewidth-size relationships from $\sigma \propto R^{1/2}$ may produce $X \approx X_{\text{Gal}}$.

In models with random velocities having 1D dispersions

¹⁰ <https://people.ok.ubc.ca/erosolo/dendro.html>

¹¹ We use the \hat{z} -component since the CO emission is calculated for the \hat{z} -direction.

¹² These LoS velocity dispersions include a contribution from the 0.5 km s^{-1} microturbulent velocity, so are not exactly equal to $v_{\text{rms}}/\sqrt{3}$.

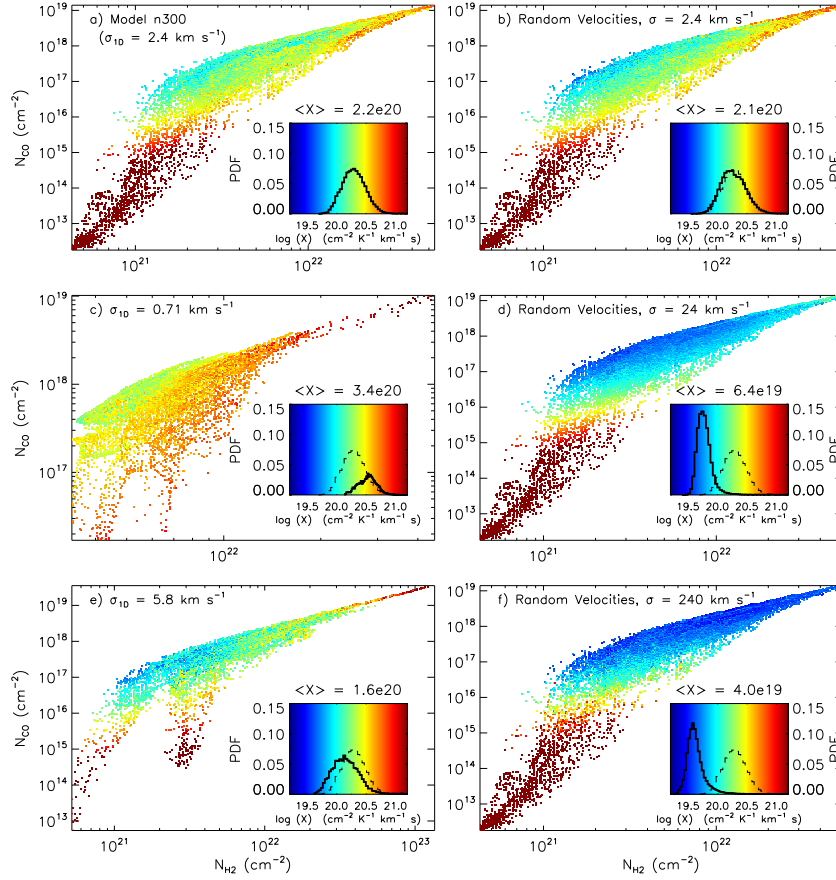


Figure 14. The variation of the X factor with N_{H_2} and N_{CO} , as in Fig. 8, but for models with different internal velocity fields. a) Original model n300, which has $\sigma_{1D}=2.4 \text{ km s}^{-1}$, b) model n300, but with velocities replaced from a Gaussian distribution with $\sigma=2.4 \text{ km s}^{-1}$, c) model with $\sigma_{1D} = 0.71 \text{ km s}^{-1}$ ($v_{\text{rms}}=1 \text{ km s}^{-1}$), d) n300, but with Gaussian velocities with $\sigma=24 \text{ km s}^{-1}$, e) model with $\sigma_{1D} = 5.8 \text{ km s}^{-1}$ ($v_{\text{rms}}=10 \text{ km s}^{-1}$), and f) n300, but with Gaussian velocities with $\sigma=240 \text{ km s}^{-1}$. In b)-e), the X factor distribution from the fiducial n300 model in a) is shown as the thin dashed histogram. The emission weighted X factor $\langle X \rangle$ is indicated in each panel.

$\sigma=24$ and 240 km s^{-1} , the X factor is systematically lowered, to $\langle X \rangle = 6.4 \times 10^{19}$ and $4 \times 10^{19} \text{ cm}^{-2} \text{ K}^{-1} \text{ km}^{-1} \text{ s}$, respectively. *Therefore, the integrated CO intensity W is not sensitive to the velocity structure, but only the extent of the range in velocities.* This occurs because with larger velocity differences between regions along a LoS, more CO line photons are able to escape the cloud and ultimately be detected, resulting in an increase in W . Increasing Δv thereby effectively reduces the percentage of mass that has $\tau > 1$ (and is therefore “invisible”), so that more CO becomes visible. Notice that the difference in the X factors of the models with dispersions of 24 and 240 km s^{-1} (Fig.14d and f) is modest. Thus, X does not simply scale inversely with σ . In fact, the results from models with $\sigma = 2.4, 5.8$, and 24 km s^{-1} show a behavior closer to $X \propto \sigma^{-1/2}$ than $X \propto \sigma^{-1}$. We return to this point in Section 4.6.

Of course, the range in velocities must be sufficiently well-sampled, so that there are no significant velocity gaps, which will indeed be the case in MCs. The $\sigma=24$ and 240 km s^{-1} models have a large range in velocities, and consequently, likely have under-resolved velocity gradients. In the Appendix, we discuss how radiative transfer calculations may provide inaccurate intensities in regions where the ve-

locity gradients are poorly resolved, and how our analysis accounts for this effect.

4.5 Does “cloud counting” result in a constant X factor?

One explanation for the lack of variation in the X factor in the Galaxy is that the integrated CO intensity is a measure of the number of optically thick “cloudlets” along the LoS, hereafter LoS. This is known as the “mist” model proposed by Solomon et al. (1987). Since we have knowledge of all the relevant quantities affecting the X factor, we can test this idea by inspecting the characteristics of the gas contributing to the observed emission.

Figure 15 shows the spectrum from two LoSs. The top panels show T_B and τ at each spectral channel. The bottom panels show the corresponding volume density and velocity. For reference, the observer is situated beyond LoS position 0 in panels c-d, so that observed line photons are traveling from high LoS position towards lower LoS position (to the left on the plots).

Both LoSs A and B have similar total column densities, 1.0 and $1.1 \times 10^{20} \text{ cm}^{-2}$, respectively. However, the inte-

grated intensities differ by a factor of ~ 2.5 . Perhaps surprisingly, LoS A, which has slightly lower column density, has a much higher intensity. As a result of this difference in W , the resulting X factors for these LoSs as computed from Equation 1 also differ.

The differences in the total intensities and line shapes from the LoSs depicted in Figures 15a-b can be understood by inspecting the density and LoS velocity distribution shown in Figures 15c-d. LoS A has relatively low density gas $\lesssim 100 \text{ cm}^{-3}$ in the majority of positions along the LoS, at position 0-17 pc. Near LoS position 17 pc, there is a sharp jump in density, and an associated perturbation in velocity. The lowest LoS velocities associated with this shock, $\lesssim -5 \text{ km s}^{-1}$, are unique to this particular region along the LoS - no other region along this LoS has similar velocities. Accordingly, observed emission in the -5 to -7 km s^{-1} range originates from this high density, optically thick cloudlet. Emission at velocities -3 to 4 km s^{-1} from this cloudlet may be absorbed by the gas lying along the LoS with similar velocities. However, this gas has very low column density, and so in fact does not significantly attenuate the emission from the shock. Thus, the whole line profile in the -7 to 3.5 km s^{-1} range is due to the high density shock. Only the weak remaining emission at velocities $\gtrsim 4 \text{ km s}^{-1}$ is due to gas at positions $\lesssim 3 \text{ pc}$. We discuss some numerical effects in regions of such high velocity contrast in the Appendix.

The LoS in Figures 15b does not have any gas with $n_{\text{H}_2} > 2000 \text{ cm}^{-3}$. There are numerous optically thick regions, with a significant overlap in velocities. Some regions, such as the peak near position 8 pc, have small velocity gradients, while others contain a large range in velocities, as the peak near position 14 pc. Due to the large overlap in velocities, especially at -4 km s^{-1} , the integrated optical depth reaches very high values up to 170. The combination of velocity overlap and lower density gas results in LoS B having a lower integrated intensity than LoS A.

Figure 16 shows two other LoSs with lower column densities; these have equivalent $N_{\text{H}_2} = 3.5 \times 10^{21} \text{ cm}^{-2}$. Yet, the integrated intensity varies by a factor of ~ 3 , resulting in an equivalent discrepancy in the X factor. Judging by the optical depth profile, there appears to be either one or two cloudlets. However, the detailed velocity and density profiles show that the structure is much more complex.

Almost all of the gas along LoS C has densities $\gtrsim 10 \text{ cm}^{-3}$. Most of the gas velocities, especially those associated with the density peaks with $n_{\text{H}_2} \gtrsim 100 \text{ cm}^{-3}$, lie in the range -3 to -1 km s^{-1} . There are many density peaks with overlapping velocities, but the resulting line profile has only three peaks. Since $\tau > 1$, the observed intensity at a given velocity emerges from the last density peak along the LoS with the given velocity. Thus, much of the emission from LoS position $> 10 \text{ pc}$ is absorbed. By rerunning the radiative transfer on this LoS by excluding some of the gas, we have verified that a significant number of CO line photons are absorbed. We provide examples demonstrating this scenario in Section 4.6.

For LoS D, a fraction of the gas has $n_{\text{H}_2} \lesssim 10 \text{ cm}^{-3}$. This LoS has two well defined peaks in the line profile. These peaks are centered on -3 and 3 km s^{-1} . At those velocities, there are two distinct cloudlets with $n_{\text{H}_2} \gtrsim 1000 \text{ cm}^{-3}$. Clearly, the emission from LoS D comes from the most dense regions along the LoS. Since they are well separated in ve-

locity, both are easily detected and contribute to a larger integrated intensity than LoS C.

The comparison of observed profiles, densities, and velocities in Figures 15 and 16 suggest that the simple “mist” model does not accurately capture the complexity intrinsic to line radiative transfer from a turbulent medium. In the comparison of LoS A and B in Figure 15, both of which have a large N_{H_2} , A has one true cloudlet with very high density. This cloudlet is only present in a localized region along the LoS, but contains a large range in velocities, and therefore is the source of most of the observed emission. Other emitting regions with different velocities only contribute slightly to the spectrum, due to their significantly lower densities. LoS B has numerous lower density cloudlets, many of which have similar velocities. The integrated intensity is lower, though the total amount of gas along this LoS is slightly larger than LoS A.

In the comparison of low density LoSs in Figure 16, both LoSs have a few regions with clear density peaks. However, the dominant cloudlets in LoS D have larger density, and span a larger range of velocities. Thus, LoS D has a higher total intensity than LoS C even though the total column density in both LoSs are equivalent.

The “mist” model would predict that LoSs with more high density cloudlets would have higher integrated intensities, since the cloudlets are separated in velocity. However, comparison of LoS A and B show the opposite: one very dense cloudlet with a large velocity gradient may be responsible for the whole LoS profile. This integrated intensity W may be larger than that from a different LoS with a larger number of cloudlets, but nevertheless a similar total column density and total velocity width. Further, two LoSs with equivalent N_{H_2} and similar number of cloudlets may have different W if one LoS has overlapping cloudlets in velocity space, while the other LoS has well distributed cloudlets in velocity space. This effect is partly at work in the comparison of LoS C and D in Figure 16.

We have shown that in a turbulent medium, emitting cloudlets do in fact overlap in velocity space (see also Ballesteros-Paredes & Mac Low 2002; Shetty et al. 2010), and that individual cloudlets may have a range in velocities, thereby dominating the emission at all velocities in that LoS. These factors all compromise any simple relation between W and N_{H_2} , and therefore any direct scaling between X and N_{H_2} . Of course, this analysis considers individual LoSs through a molecular cloud, whereas the idea of a constant X factor is usually discussed in the context of whole molecular clouds. Accordingly, we next consider the cloud-averaged CO spectrum.

4.6 Cloud-averaged X factor and spectra

Figure 17 shows the averaged spectrum for the whole n300 cloud model, as well as model n300 where the velocities are manually replaced with $\sigma = 24 \text{ km s}^{-1}$ (see Fig. 14d). Each point shows the mean brightness temperature of each channel in the synthetic observation. The integrated intensity of this spectrum is $W = 40.2$ and $137.5 \text{ K km s}^{-1}$ for the fiducial and velocity-altered model, respectively.

The best fit Gaussians to the averaged spectra are also shown in Figure 17. The spectra are very well fit by Gaussians. Using the peak and dispersion of the Gaussian fit, the

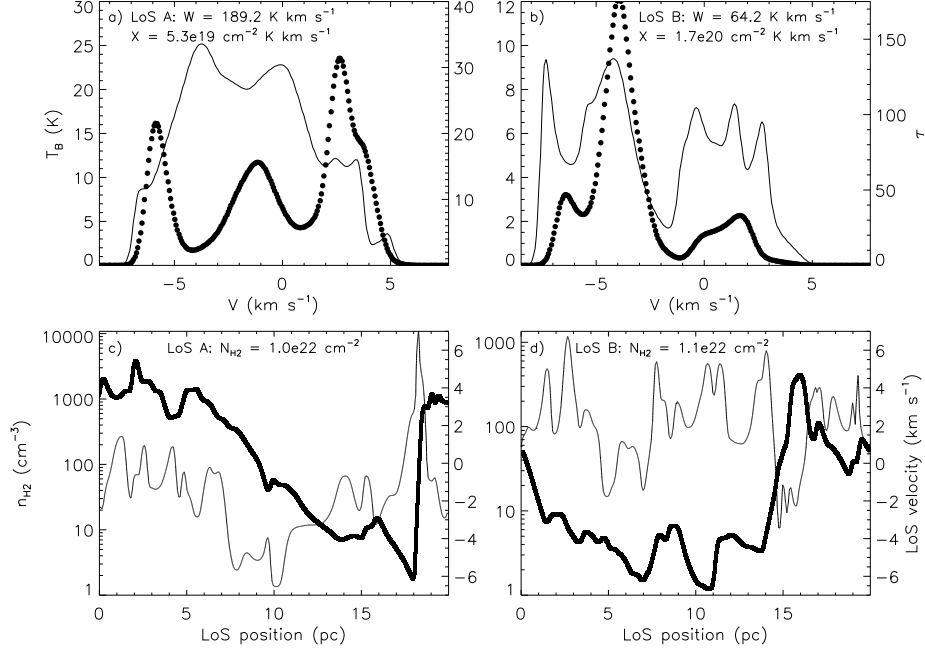


Figure 15. Top panels - CO spectra (lines - left axis) and optical depth (circles - right axis), and bottom panels - H₂ column densities (thin - left axis) and LoS velocities (thick - right axis) from two LoSs in the n300 simulation. The corresponding integrated intensities and X factors are listed in a-b, and the column densities are listed in c-d.

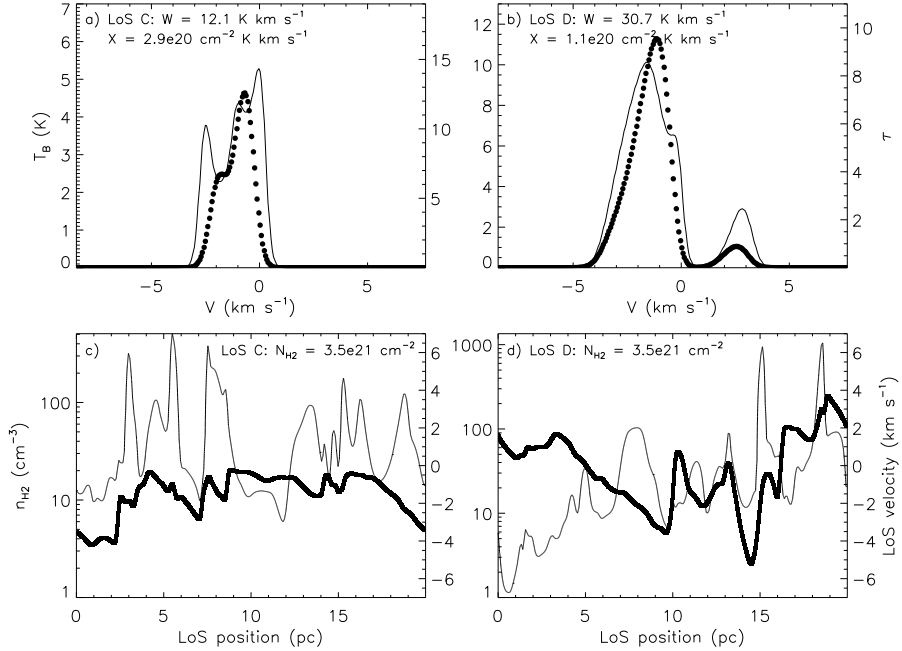


Figure 16. Similar to Fig. 15, but for different LoSs. The column density of both LoSs are equivalent.

corresponding integrated intensities reproduce the true integrated intensities. Using W along with the mean column density $\overline{N}_{H_2} = 9.0 \times 10^{21}$ cm⁻² in Equation 1 results in $X = 2.2 \times 10^{20}$ and 6.5×10^{19} cm⁻² K⁻¹ km⁻¹ s for the original and 24 km s⁻¹ models, respectively. These values of the X factor are equivalent to the emission-weighted mean X found in Section 4.1 and listed in Figure 14. The X factor value for n300 is nearly identical to the reference value in Ta-

ble 1. For the altered velocity model, $\langle v_z^2 \rangle_{mass} = 24$ km s⁻¹ so the reference $\langle X \rangle_{ref} = \langle n_{H_2} \rangle_{vol} L / [\langle T \rangle_{mass} (\langle v_z^2 \rangle_{mass})^{1/2}] = 1.9 \times 10^{19}$ cm⁻² K⁻¹ km⁻¹ s. This value is significantly lower than X determined by the spectrum, largely due to the fact that $T_B / \langle T \rangle_{mass}$ is a factor 3 lower for the 24 km s⁻¹ model than for model n300 with $\sigma_{1D} = 2.4$ km s⁻¹. Therefore the mass-weighted quantities $\langle T \rangle_{mass}$ and $\langle v_z^2 \rangle_{mass}^{1/2}$, cannot fully account for W . We note that the line widths of the

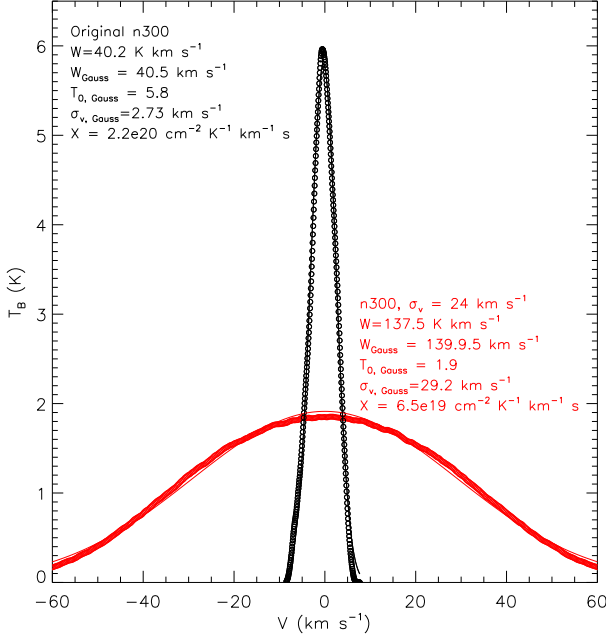


Figure 17. Averaged spectrum from model n300 (black), and model n300 for which the velocities were replaced from a random distribution with $\sigma = 24 \text{ km s}^{-1}$ (red). Lines show best fit Gaussians. Integrated intensity, fit Gaussian parameters, and X factor, are listed for both models.

observed spectrum are slightly larger than the intrinsic velocity dispersion. This is due to some extent to our choice of the microturbulence, which we discuss in more detail in the Appendix.

The cloud-averaged spectra in Figure 17 show very smooth profiles, and do not demonstrate any of the variability seen along individual LoSs. Clearly, the cloud with a larger velocity dispersion is brighter because the emission from more gas with a larger dispersion is able to escape the cloud. Even though both models have the same mass, their integrated emission differs by a factor 3.4. This is due to a combination of a larger velocity dispersion (by a factor ~ 10), and a lower peak brightness temperature (by a factor ~ 3) for the 24 km s^{-1} model compared to model n300. As a result, use of the integrated intensity alone, or any X factor, would provide inaccurate mass estimates.

We have demonstrated that there is no simple relationship between W and N_{H_2} in highly turbulent clouds (see also Paper I). This lack of correlation is due to the combination of the optically thick nature of CO, and the complexity in the structure of CO bright regions: emitting gas along individual LoSs sometimes overlaps in velocity space and sometimes does not, and even lower density gas not necessarily found in cloudlets contributes significantly to the observed intensity. Under such circumstances, there should be significant amounts of gas that is untraceable in the CO line.

Figure 18 shows the averaged spectrum of three models. The black spectrum is from the original n300 model. The red and blue points show the results of the radiative transfer calculations from model n300, but only when gas with $n_{\text{H}_2} < 1000 \text{ cm}^{-3}$ and $> 1000 \text{ cm}^{-3}$ is included in the calculation,

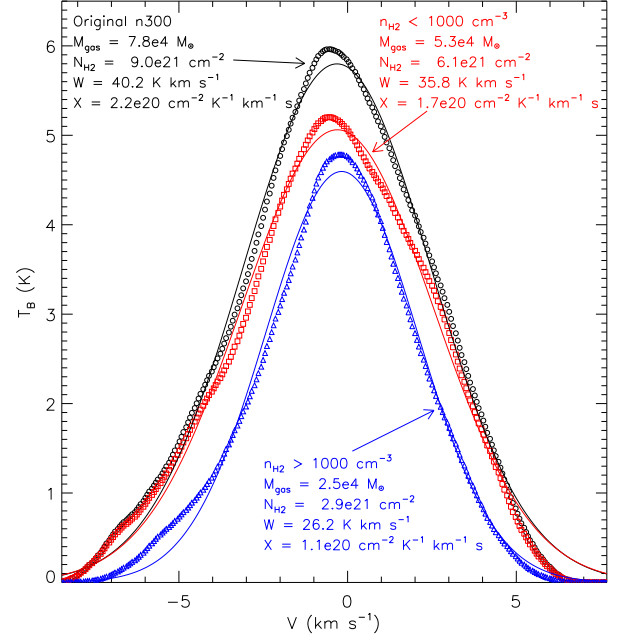


Figure 18. Averaged spectrum from original model n300 (black circles), along with spectrum from the original model but only gas with $n_{\text{H}_2} < 1000 \text{ cm}^{-3}$ (red squares) and $> 1000 \text{ cm}^{-3}$ (blue triangles) is considered. Lines show best fit Gaussians.

respectively. The CO and H_2 density is set to zero in zones with $n_{\text{H}_2} < 1000 \text{ cm}^{-3}$ or $> 1000 \text{ cm}^{-3}$, respectively.

The gas mass in the model that has $n_{\text{H}_2} < 1000 \text{ cm}^{-3}$ is $5.3 \times 10^4 M_{\odot}$, which is roughly 2/3rds of the total mass in the original n300 model. However, the integrated intensity from this model is 90% of that from model n300. The total mass at $n_{\text{H}_2} > 1000 \text{ cm}^{-3}$, $2.5 \times 10^4 M_{\odot}$, accounts for the remaining 1/3 of the mass in model n300. But the integrated intensity from this model is 26.2 K km s^{-1} , which is 65% of the total W of the original model.

Due to the significant amount of self-absorption occurring in both low density and high density gas, removing some gas simply allows other gas along the LoS to become “visible.” There are LoSs where some CO emitting regions go completely undetected, since other optically thick gas lying in the same LoS with similar velocities will absorb its emission. Consequently, a spectrum from a given LoS may depend on the observing direction. For example, if the observer were located at LoS position $> 20 \text{ pc}$ in Figures 15 and 16, instead of at LoS position $< 0 \text{ pc}$, the spectra may have different profile shapes. We have indeed found such discrepancies in many LoSs. This is further confirmation that there is no simple correlation between N_{H_2} and W . We stress again that the use of a constant X factor for numerous clouds will not provide reliable estimates of the molecular mass.

5 DISCUSSION

5.1 Why is the Galactic X factor found to be nearly constant?

After investigating the dependence of the X factor on the physical characteristics of synthetic MCs, we are now in a position to interpret the observed trends, as well as compare our results with previous efforts.

For our model with Milky Way parameters, we have demonstrated that under certain conditions, using the mass-weighted mean values of temperature and velocity dispersion may provide reasonably good estimates of X factor. Thus, it might seem unsurprising that systems with similar mass-weighted temperatures or velocity dispersions are able to reproduce the X factor from the original model. By exploring models with different temperatures and velocities, however, we find that $X_{ref} = \langle N_{H_2} \rangle / (\langle T \rangle_{mass} \sigma_{v,los})$ does not in general agree with the value of $\langle X \rangle = N_{H_2} / W$ computed from radiative transfer models. Further, $\langle X \rangle$ does not simply depend on the inverse of the temperature or velocity.

Even though the experiments testing the variation of a constant kinetic temperature on the CO line do not self-consistently follow the coupling of other MC properties with T , we may compare our results with previous investigations. We find that $X \propto T^{-0.5}$, which is a weaker $X-T$ dependence than the $X \propto T^{-1.3}$ behavior found by Kutner & Leung (1985). Their models have velocities which are dominated by microturbulence, but nevertheless obey the empirical linewidth-size relationship. We find that microturbulence does not significantly affect the integrated intensity, nor correspondingly the X factor (see Appendix showing profiles with different microturbulent velocities). In our models, the CO intensity is more sensitive to the macroturbulent velocities.

Thus, our results are in closer agreement to the investigation by Wolfire et al. (1993), who find that macroturbulent or clumpy models are better able to reproduce observed line profiles than microturbulent models. However, a key difference between our model and that of Wolfire et al. (1993, as well as Dickman et al. 1986) is that in their clumpy models, much of the CO emission emerges from distinct optically thick clumps. Further, their models require approximately one clump along each LoS at a given velocity in order to reproduce observed spectra.

The Wolfire et al. (1993) models are conceptually similar to the “mist” model often employed to explain the constant X factor (Dickman et al. 1986; Solomon et al. 1987) and described in Section 4.5. In our turbulent models, only the cloud-averaged CO linewidths provide accurate measures of the total (1D) velocity dispersion. Along an individual LoS, the line shape is strongly dependent on the density and velocity structure. We find that though dense gas is responsible for much of the observed CO emission globally, along individual LoSs diffuse gas may also be a significant source. Depending on the gas velocities along the LoS, lower density regions may also be optically thick, and so may contribute substantially to the emergent intensity.

One of the key results of our work is that the X factor is insensitive to the detailed linewidth – size relationship in the cloud. In Section 4.4 we demonstrated that a cloud consisting of gas with random velocities has an almost identical X factor distribution with a cloud that has a well defined

$\sigma \propto R^{\frac{1}{2}}$ linewidth-size relationship. This suggests that the linewidth-size relationship has very little influence in determining the X factor, or W . The lack of dependence of W on the detailed velocity structure suggests the use of a representative velocity width for the $\int dv$ term in Equation 4. Although linewidths computed from the mean spectrum may differ slightly from $\langle v_z^2 \rangle_{mass}^{1/2}$, a more significant effect of radiative transfer is to reduce T_B when the velocity width increases. Consequently, we find that W does not increase linearly with the velocity dispersion. In particular, we find that an increase of the velocity width by a factor 10 or 100 only reduces $\langle X \rangle$ by a factor 3 or 5 relative to model n300 (see caveats in Appendix).

Along with N_{H_2} , W determines the X factor through its traditional definition given by Equation 1. Based on our tests, for $N_{H_2} \sim 10^{22} \text{ cm}^{-2}$, the X factor can only vary by a factor $\lesssim 5$, given the limited range of dense-gas temperatures 10 - 25 K and velocities ~ 2 - 5 km s^{-1} observed for Galactic MCs (e.g. Solomon et al. 1987; Roman-Duval et al. 2010). The mass-size relationship proposed by Larson (1981) implies a constant mean column density in MCs. Recent observations have challenged the notion that all MCs have column densities, averaged over large scales, similar to one another (Heyer et al. 2009; Kauffmann et al. 2010b). Nevertheless, column densities are not expected to vary significantly from cloud to cloud, and they generally fall in the range from 10^{21} – 10^{22} cm^{-2} . Structures with much lower column densities than $\sim 10^{21} \text{ cm}^{-2}$ probably would not be observed as *molecular* clouds, as there would be insufficient CO to be detected. Clouds with column densities much larger than $\sim 10^{22} \text{ cm}^{-2}$ would be very gravitationally unstable - rapid collapse, fragmentation, and the destructive effects of star formation would all prevent clouds from maintaining such high column densities over long periods of time (within an environment of much lower mean density and column density). Thus, we believe the limited range in N_{H_2} , velocity dispersion, and MC temperature together explain the limited range in the X factor found by numerous observations of Galactic MCs.

5.2 Does a constant X factor require virialized clouds?

A common interpretation of the limited range in X factors from observations of Galactic MCs is that they are “virialized” objects. The “mist” model of Solomon et al. (1987) invokes the “virialized” cloud depiction to explain the limited range in the measured virial mass - CO luminosity (M_{VT}/L_{CO}) ratio. Generally, a mass-to-luminosity ratio, α , is simply the X factor written in terms of a gas mass and CO luminosity, instead of N_{H_2} and W , so that $X = 4.5 \times 10^{19} \alpha$ if α has the units $M_{\odot}/(\text{K km s}^{-1} \text{pc}^{-2})$. Since the derivation of a constant $\alpha_{VT} \equiv M_{VT}/L_{CO}$ for virialized clouds has been presented in numerous works (e.g. Solomon et al. 1987; Maloney 1990; Young & Scoville 1991), we only briefly outline these arguments, and then discuss how our models relate to such a description.

For a cloud in virial equilibrium, the internal velocities are fully governed by the gravitational field due to the gaseous mass,

$$\sigma_{VT}^2 \equiv \frac{GM_{VT}}{5R}. \quad (8)$$

Here, we have used “VT” to label the one-dimensional virial velocity width σ_{VT} , and the factor 5 assumes a spherical, uniform cloud (Bertoldi & McKee 1992). Note that in this notation, σ_{VT} is the 1D velocity dispersion (assuming an isotropic distribution), whereas σ refers to the observed linewidth along the LoS.

Cloud-averaged spectra often have Gaussian shapes, so that the CO luminosity can be computed using the Gaussian line parameters $T_{B,0}$, the peak brightness temperature, and linewidth σ , along with the projected area πR^2 :

$$L_{CO} = \sqrt{2\pi} T_{B,0} \sigma \pi R^2. \quad (9)$$

Taking Equations 8 and 9 together, and assuming $\sigma = \sigma_{VT}$,

$$\alpha_{VT} \equiv \frac{M_{VT}}{L_{CO}} \propto \frac{\sigma/R}{T_{B,0}}. \quad (10)$$

Using Equation 8, $\sigma/R \propto (GM/R^3)^{1/2}$ so that Equation 10 is equivalent to

$$\alpha_{VT} \equiv \frac{M_{VT}}{L_{CO}} \propto \frac{\rho^{1/2}}{T_{B,0}}. \quad (11)$$

If ρ and $T_{B,0}$ take on a limited range of values, this yields an approximately constant α_{VT} and X .

When further combined with an empirical linewidth-size relation $\sigma \propto R^{1/2}$, equation 8 yields

$$M_{VT} \propto \sigma^4, \quad (12)$$

and equation 9 yields $L_{CO} \propto T_{B,0} \sigma^5$. These relations combine to give

$$M_{VT} \propto \left(\frac{L_{CO}}{T_{B,0}} \right)^{0.8}. \quad (13)$$

CO observations are often used to obtain cloud masses through Equation 8, assuming $\sigma = \sigma_{VT}$. Such an analysis usually produces a strong correlation between M_{VT} and L_{CO} , with a power law index 0.8. Though we have only followed proportionalities in Equations 10 - 13, it is straightforward to consider the coefficients explicitly (e.g. Maloney 1990; Solomon & Vanden Bout 2005). The observed $M_{VT} - L_{CO}$ trend also results in good agreement in these coefficients. The agreements in both the power law exponents and coefficients are often taken as evidence that MCs are virialized objects, and that N_{H_2} is approximately constant for MCs, since $N_{H_2} \propto \Sigma \propto M/R^2 \sim \text{constant}$ if $\sigma^2 \propto M/R$ and $\sigma \propto R^{1/2}$.

The apparent agreement between the observed M_{VT}/L_{CO} and the analytical derivation outlined above depends on two crucial assumptions, the mass-size and linewidth-size relations. As discussed above, numerous observations demonstrate a $\sigma \propto R^{1/2}$ relationship over a range of scales for MCs (Larson 1981; Solomon et al. 1987; Bolatto et al. 2008). However, recent analysis by Heyer et al. (2009) of higher resolution observations of the clouds studied by Solomon et al. (1987) found that the coefficient of the linewidth-size relationship may not be constant. Furthermore, the observed mass-size relationship $M \propto R^2$ is rather uncertain. Using observations of MCs in ^{12}CO and ^{13}CO , which should trace more of the cloud gas due to the lower optical depth, Roman-Duval et al. (2010) find an exponent of 2.4 rather than 2. By assessing the mass on a continuous range of scales in a number of Galactic MCs, Kauffmann et al. (2010a,b) found

no universal power law mass-size relationship. Additionally, when optically thin (e.g. dust) observations are employed, projection effects may lead to overestimated masses (Ballesteros-Paredes & Mac Low 2002; Gammie et al. 2003; Shetty et al. 2010). Another potential issue is that the definition of cloud size R may affect any M estimates. Usually, the size R is set to the radius of a circle with area equivalent to that of the projected area of the cloud. Using a different definition of R may result in an altered mass-size relation, and possibly even a different linewidth-size relation. These caveats will all affect any derived mass - luminosity correlations.

In this paper, we have studied CO emission from turbulent MC models which do not have self-gravity, and thus are not “virialized.” Nevertheless, the virial mass inferred from the synthetic CO observation accurately recovers the cloud mass ($7.8 \times 10^4 M_\odot$) to within 1%, for the n300 model. Since the parameters adopted for the n300 model were designed to represent Milky Way MCs, this agreement may lead to the spurious inference that the MC is “virialized.” Additionally, we have found that the integrated emission, and hence the X factor for the adopted value of N_{H_2} , is insensitive to the velocity structure (see Section 4.4). As a result, a cloud with $\sigma \gg \sigma_{VT}$ or $\sigma \ll \sigma_{VT}$ which is far from “virialized” could still have quite similar X values to a cloud with $\sigma \sim \sigma_{VT}$. Consequently, our analysis supports the arguments put forth by Maloney (1990) and Combes (1991) that a constant X factor does not require MCs to be “virialized.”

In effect, our analysis shows that $X \sim X_{\text{Gal}}$ is simply a result of the limited range of both the numerator and denominator of Equation 4, or of the parameters entering the right hand side of Equation 10 or 11 for gravitationally-bound MCs: the densities, brightness temperatures, and (observed) velocities. Only if the velocities are governed solely by gas self-gravity through Equation 8 and a universal linewidth-size $\sigma \propto R^{1/2}$ relationship holds can a (nearly) constant M_{VT}/L_{CO} ratio be expected for all MCs. The linewidths of observed clouds, which measure the internal motions, may or may not be set solely by gas self-gravity. An additional caveat is that the Equation 8 may not be sufficient for identifying the dynamical state of a cloud, since it does not account for surface, magnetic and time-varying terms in the virial equation (Ballesteros-Paredes 2006).

5.3 Future work: X factor in molecular dominated regions

For molecular environments different from Milky Way GMCs, the different (volume and column) densities, velocities, and/or temperatures, should contribute to a variation in the corresponding X factors. As indicated in the previous section, we have focused on one model with densities similar to those of Milky Way MCs. Molecular dominated regions such as ULIRGs and the Galactic center have much higher column densities, in addition to elevated temperatures and observed velocity dispersions, so the results found in this work are not directly applicable to those sources. In this section, we briefly explore the results from the previous section in the context of ULIRGs, and motivate an analogous study of higher column density models.

In molecular dominated regions, the X factor is believed to be lower than X_{Gal} (see e.g. Fig. 1, Tacconi et al. 2008).

In part, this is because the standard value of X_{Gal} yields molecular masses that are sometimes larger than the dynamical masses of the galaxies. In order to avoid this unphysical situation, Downes et al. (1993) proposed that the masses traced by CO observations of ULIRGs are not the virial masses, but rather the geometric mean of the gas and dynamical masses, i.e. $L_{\text{CO}} \propto T_{\text{B},0}(M_{\text{gas}}M_{\text{dyn}}/\rho_{\text{gas}})^{1/2}$. In their interpretation, the CO linewidths trace the dynamical masses of the starbursting, molecular rich systems. Thus, the virial velocities and masses in Equation 8 must be replaced by the dynamical velocities and masses of ULIRGs. Instead of using $\alpha_{\text{VT}L_{\text{CO}}}$ (Eqn. 11) to estimate masses, one can estimate the product of dynamical and gas mass of ULIRGs through $(\alpha L_{\text{CO}})^2$, where $\alpha = 2.6n_{\text{gas}}^{1/2}/T_{\text{B},0}$ (Eqn. 5 in Solomon & Vanden Bout 2005). The ratio $M_{\text{gas}}/L_{\text{CO}}$ computed from ULIRGs is $\sim 3 - 6$ times lower than that estimated from MCs (e.g. Solomon & Vanden Bout 2005).

ULIRGs have observed CO linewidths of the order of a few hundred km s^{-1} (e.g. Solomon et al. 1997; Downes & Solomon 1998). Since the molecular component of ULIRGs are inclined rotating disks, the observed CO linewidths are primarily tracing the rotational motion of the molecular-dominated ISM. Downes & Solomon (1998) find that turbulent velocities of ULIRGs must be significantly higher than Galactic MCs in order to accurately fit their observed lines. However, due to the compact extent of ULIRGs and the high optical depth of CO, accurately separating the turbulent and rotational contributions to the observed linewidths is not trivial.

The observed brightness temperatures of ULIRGs are significantly lower than Galactic MC values. However, ULIRG kinetic temperatures can be $\gtrsim 10$ times larger due to enhanced star formation activity (e.g. Solomon et al. 1997). In Section 4.6, we showed that the brightness temperature indeed decreases with increasing velocity dispersion. Accurately quantifying this $T_{\text{B}}-\sigma$ relationship calls for more realistic models which self-consistently contain higher temperature, higher dispersion, and have sufficiently high resolution (see Appendix).

In Section 4.4, we showed that a model with random velocities with dispersion 240 km s^{-1} , similar to the values found from ULIRGS, produces $X = 4.0 \times 10^{19} \text{ cm}^{-2} \text{ K}^{-1} \text{ km}^{-1} \text{ s}$. In addition, we found $X = 7.9 \times 10^{19} \text{ cm}^{-2} \text{ K}^{-1} \text{ km}^{-1} \text{ s}$ for the $T=100 \text{ K}$ model from section 4.2. These X factor values are a factor ~ 3 -5 lower than X_{Gal} and the value found from the original n300 model, and are consistent with X factor estimates from ULIRG observations. These could be due to either extremely high small-scale turbulent velocity dispersions (as experienced by photons escaping from the molecular disk) and moderate gas temperatures, or much higher gas temperatures and moderate small-scale turbulence combined with very large non-circular motions on $10^2 - 10^3 \text{ pc}$ scales (still within the typical beam size for molecular observations, but larger than the molecular disk thickness). We note that none of our current models has column densities comparable to ULIRGS. The effects of higher star formation, very high density and total column density, and rotation all need to be studied in detail to understand the CO- H_2 conversion factor from ULIRG systems. More detailed modeling should quantify the contribution of rotational and turbulent velocities, along with other physical properties in setting the X factor of ULIRGs. Efforts con-

sidering such environments are currently underway (current authors, and Narayanan et al. in prep).

6 SUMMARY

6.1 Overview: Interpreting the X factor

By performing radiative transfer calculations on model MCs, we assess the physical properties which are most responsible for setting the X factor, the ratio of molecular column density to integrated CO intensity. The fiducial model MC is a result of a magnetohydrodynamic simulation of a gaseous medium responding to driven turbulence with a treatment of chemistry which tracks the formation and destruction of H_2 and CO; the resulting MC has many properties similar to those found in Galactic MCs (Section 3 and Paper I). After discussing the X factor from the fiducial model, we modify the physical characteristics of the model MC and recompute the emerging CO line emission from the altered models. We then compare the modified X factor with that provided by the original model (Section 4), and discuss our results in the context of observed trends (Section 5).

Our analysis was aimed at understanding the limited range in the X found from Galactic MC observations, shown in Figure 1. We discussed the trend of a higher X factor for low density regions in Paper I. Basically, environments with lower CO densities have lower CO intensities. This could be due to lower total density, higher background UV radiation fields, or lower metallicities. Though Σ_{gas} in the simulations ranges between ~ 50 -500 $\text{M}_{\odot} \text{ pc}^{-2}$, and the X factor along individual LoSs can vary significantly, in all except the very low metallicity models the cloud-averaged $\langle X \rangle \sim X_{\text{Gal}}$ (see Fig. 2). In this work, we have found that it is the limited range in velocities and temperatures that constrains W , and thereby X , for a given column density.

This interpretation applies for systems above a threshold column density beyond which CO is optically thick ($\sim 20 \text{ M}_{\odot} \text{ pc}^{-2}$), but below very high column densities commonly found in ULIRGs. The precise value of the threshold column density depends on a number of environmental factors of the source, such as the metallicity, UV radiation intensity, and dust density. Below this column density, CO is optically thin, so a small decrease in column density results in a stronger decrease in CO intensity W , and thereby an increase in X . At larger column densities, CO is optically thick. Thus, an increase in CO abundance may or may not lead to an increase in CO intensity, depending on the distribution of gas velocity. Much larger CO column densities are usually found in molecular rich sources such as ULIRGs, which generally have higher temperatures, total densities, as well as observed velocity dispersions (due to rotation and/or turbulence) – conditions which are not self-consistently followed in the models presented here.

An important consequence of our conclusion is that a given X factor value may not always provide an accurate mass estimate of MCs detected from CO observations. Observationally, X factor relations between total mass and CO brightness may coincidentally work well over suitably large areas of molecular clouds. This may simply reflect the limited range in the mean column density, temperature, and velocity dispersion within typical MCs. These underlying global properties of the emitting regions make a bridge

between the average of many LoSs with individual LoSs, where the relationships generally fail. MC masses estimated through a chosen constant X factor should only be thought of as a first approximation of the gas mass, to within $\sim 50\%$. Indeed, that derived X factors for Galactic MCs themselves vary by up to a factor of five has already been a warning sign that a universal CO luminosity to gas mass conversion does not exist (e.g. Solomon et al. 1987; Oka et al. 1998; Pineda et al. 2008, and Fig. 1). Due to its high optical depth, there may be a significant amount of CO self-absorption. As a result, CO intensities only provide rough estimates of the gas mass.

6.2 Main Results

1) We find a roughly constant X throughout the model MC only when the CO intensity is integrated over all velocities. When intensities at each PPV location are considered along with the column density $N_{\text{H}_2, \nu}$ associated with that PPV position, there is a clear trend of an increasing X factor with increasing column density. This occurs because in high density regions the CO line is saturated, so increasing the column density only leads to more self-absorption, resulting in an increase in the column density - CO intensity ratio (Section 4.1).

2) The variation in X between different LoSs through an individual cloud is not due to the variation in temperature within the MC. When setting the temperature to the mass-weighted average value, the original X factor distribution is recovered. The cloud-averaged X factor is thus determined primarily by the densest regions in the MC. We find a weak dependence of X on T : roughly $\langle X \rangle \propto T^{-0.5}$ from 20 K to 100 K if density and velocity structure are fixed (Section 4.2).

3) Even though the X factor is defined with a column density, it also depends on the volume density n_{H_2} . This is due in part to the saturation of the CO line at high densities, as indicated in 1) above. Increasing the mean density from $n_0 = 300$ to 1000 cm^{-3} only decreases $\langle X \rangle$ by 15%, however (Section 4.3).

4) Similarly, at high CO abundances X increases with N_{H_2} due to line saturation. At very low abundances ($f_{\text{CO}} \lesssim 10^{-6}$), the line is optically thin, so W is directly proportional to N_{H_2} producing a constant X factor. Since there is a range in CO abundances in MCs (Glover et al. 2010, Paper I), the X factor shows signatures of both high (saturation) and low opacities (Section 4.3). On average, the X factor is not strongly dependent on the f_{CO} if f_{CO} is in the observed range $\in 10^{-5} - 10^{-4}$ (Section 4.3).

5) The fiducial model MC has a linewidth-size relationship $\sigma \propto R^{1/2}$, and produces $X \sim X_{\text{Gal}}$, similar to observations. Nevertheless, the X factor from models without any linewidth-size relationship, but with a similar range in velocities, reproduces the X factor trends in the fiducial model. Further, in models with a larger range in velocities, there is less radiation trapping, leading to larger CO intensities and correspondingly lower X factors. Thus, it is the *range* in velocities that determine the X factor. The details of the velocity structure do not influence X (Section 4.4). Since the CO brightness temperature also depends on σ , the X factor does not decrease linearly with increasing σ , but in-

stead shows a variation closer to $X \propto \sigma^{-1/2}$ for $\sigma = 2 - 20 \text{ km s}^{-1}$ (Section 4.6).

6) A CO-bright LoS with a large linewidth may be due to a single high density region. Alternatively, a similar line profile may result from a LoS with numerous lower density gaseous peaks spanning a range of velocities. Therefore, two LoSs may have similar integrated intensities, but vastly different morphologies. Due to this diversity in morphology in turbulent clouds and the optically thick nature of CO, CO emission does not trace H_2 in a one-to-one fashion on individual LoSs. The “mist” model (Dickman et al. 1986; Solomon et al. 1987) does not accurately capture the complexity of turbulence and radiative transfer of the CO line in MCs (Section 4.5).

7) Similar to individual LoSs, cloud-averaged spectra do not represent the total molecular content in a one-to-one fashion. Due to the blending of numerous emitting features, the averaged CO line is Gaussian. However, in experiments where some gas is removed, the intensity of the resulting spectra is not simply scaled down by the factor that would be appropriate if CO were a linear tracer of molecular gas (Section 4.6).

8) Since we find that the X factor is insensitive to the detailed velocity structure, we argue that the reason Galactic MC observations generally find $X \sim X_{\text{Gal}}$ is due to the limited *range* in observed linewidths $\sim 2\text{--}5 \text{ km s}^{-1}$, as well as in the temperatures within dense, CO-abundant regions in MCs ($\sim 10\text{--}25 \text{ K}$, Section 5.1), and in the column densities. Thus, the nearly constant X factor found in Galactic MCs does not necessarily require that $\sigma \propto R^{1/2}$, or that clouds are “virialized.” Although a near-constant $M_{\text{VT}}/L_{\text{CO}}$ ratio would result if the velocities were governed solely by gas self-gravity, and $\sigma \propto R^{1/2}$ universally, these are not necessary conditions for X to be nearly constant, and may or may not be true for Galactic MCs (Section 5.2).

9) Given our explanation that the approximately constant $X \sim X_{\text{Gal}}$ found in Galactic MCs is due to the limited range in MC properties, masses deduced through a constant X should only be considered as a rough estimate, within a factor ~ 2 . Taking our results from Paper I and the current work together, we find cloud-averaged $X \sim 2\text{--}4 \times 10^{20} \text{ cm}^{-2} \text{ K}^{-1} \text{ km}^{-1} \text{ s}$ for Solar-metallicity models with $T \sim 10\text{--}20 \text{ K}$, velocity dispersions $\sigma \sim 1\text{--}6 \text{ km s}^{-1}$, and $= N_{\text{H}_2} \sim 2\text{--}20 \times 10^{21} \text{ cm}^{-2}$ —i.e. similar to Galactic MCs. The larger X factor values found in lower metallicity systems can be understood due to lower CO abundances (see references in Section 5.4). In molecular-dominated regions such as ULIRGs, the combined effect of higher CO and H_2 volume and column densities, higher temperatures (due to enhanced star formation), and larger velocities (due to rotation and/or turbulence) all need to be self-consistently treated to assess the X factor.

ACKNOWLEDGEMENTS

We are grateful to Desika Narayanan, Alyssa Goodman, Jaime Pineda, Mordecai Mac Low, and Jerome Pety for useful discussions on CO emission. We also thank the anonymous referee for suggestions that improved our presentation. Several of the simulations reported on in this paper were performed on the Ranger cluster at the Texas Advanced

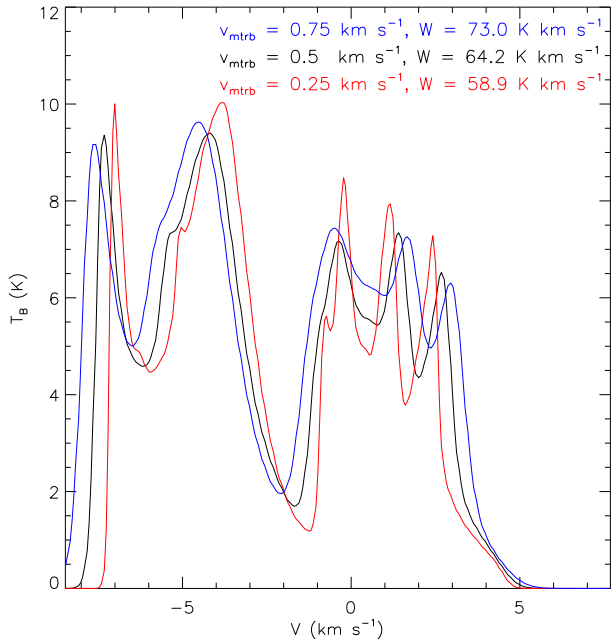


Figure A1. CO spectra from LoS B (see Fig. 15). Three different microturbulent velocities are considered: 0.25 (red), 0.5 (black) and 0.75 (blue) km s^{-1} . The velocity-integrated intensities W are indicated.

Computing Center using time allocated as part of Tera-grid project TG-MCA99S024. R.S.K. acknowledges financial support from the Landesstiftung Baden-Württemberg via their program International Collaboration II (grant P-LS-SPII/18), and subsidies from the DFG under grants no. KL1358/1, KL1358/4, KL1358/5, KL1358/10, and KL1358/11, as well as from a Frontier grant of Heidelberg University sponsored by the German Excellence Initiative. R.S., S.C.G., and R.S.K. are supported by the German Bundesministerium für Bildung und Forschung via the ASTRONET project STAR FORMAT (grant 05A09VHA). This work was supported in part by the U.S. Department of Energy contract no. DE-AC-02-76SF00515. E.C.O. acknowledges support from grant AST 0908185 from the U.S. National Science Foundation.

APPENDIX A: THE EFFECT OF MICROTURBULENCE

As indicated in Section 3 for the radiative transfer calculation, we set the microturbulent velocity $v_{\text{mtrb}} = 0.5 \text{ km s}^{-1}$ in each zone of the simulation. This value is motivated by loosely extrapolating the observed linewidth-size relationship (Larson 1981; Solomon et al. 1987) down to the physical resolution of the simulation ($\sim 0.1 \text{ pc}$). Due to observational uncertainties and the scatter in the observed linewidth-size relationship, the turbulent velocity at any given scale is not precisely known. We have thus explored how other values of v_{mtrb} may affect our results.

Figure A1 shows the spectrum from one LoS. It corresponds to LoS B shown in Figure 15. Three spectra are shown, with different values of $v_{\text{mtrb}} = 0.25, 0.5$, and 0.75 km s^{-1} .

s^{-1} . With higher microturbulence the line is broadened, and gaps or sharp features in the spectrum can become smooth, as evident near velocities of -0.5 and -5.0 km s^{-1} .

The variations in the spectra lead to slight differences in velocity integrated intensity W . For $v_{\text{mtrb}} = 0.25, 0.5$, and 0.75 km s^{-1} , $W = 58.9, 64.2$, and 73.0 K km s^{-1} . The differences in integrated intensity will of course result in corresponding differences in the X factor. For this LoS, the column density is $1.1 \times 10^{22} \text{ cm}^{-2}$, providing $X = 1.9, 1.7$, and $1.5 \times 10^{20} \text{ cm}^{-2} \text{ K}^{-1} \text{ km}^{-1} \text{ s}$. In the cloud-averaged spectra (e.g. Fig. 17), the smooth Gaussian profiles are not significantly affected, and the linewidths only vary by $\lesssim 6\%$ from the fiducial model (e.g. Fig. 17). For $v_{\text{mtrb}} = 0.25, 0.5$, and 0.75 , the peak $T_{B,0} = 5.1, 5.8$, and 6.3 K , leading to cloud-averaged X factors $2.6, 2.2, 1.9 \times 10^{20} \text{ cm}^{-2} \text{ K}^{-1} \text{ km}^{-1} \text{ s}$, respectively.

We have found that the precise value of v_{mtrb} does not affect the cloud-averaged spectrum – and the X factor – significantly. The most noticeable difference occurs in the line shapes along individual LoSs. Nevertheless, even then the differences are minimal. Any value of v_{mtrb} within the reasonable range $\in 0.25 - 0.75$ would produce very similar CO intensities. Thus, the values of the X factor found in this work, and the conclusions drawn from its analysis, would not be affected if different values of v_{mtrb} were employed.

APPENDIX B: NUMERICAL RESOLUTION

While performing radiative transfer calculations, there is a potential for obtaining inaccurate line intensities due to unresolved velocity structure. In this section, we discuss why resolving the velocity gradients is important, and how we have accounted for under-resolved velocities in our study.

In a grid-based model, the physical properties are only defined in each zone – either at the zone center or zone edge. While integrating the equation of radiative transfer, or ray-tracing, through a given LoS, the optical depth is only updated when stepping from one grid zone to the next. For a given “observed” frequency ν , corresponding to velocity v_{obs} , the optical depth τ_ν is only modified in zones with LoS velocities that correspond to the non-zero portion of the Gaussian profile function ϕ_ν (see Eqn. 7 and Eqn. 6 in Paper I).

As an example, consider the velocity profile of a sample LoS shown in Figure B1. The LoS component of the velocity v_s is only defined at discrete locations along the LoS s (e.g. edges of grid zones). At the indicated v_{obs} , due to the large velocity gradients, there would be no emission (or, if optically thick, absorption) from this region, since none of the velocities overlap with v_{obs} . Of course, if the (Gaussian) width of ϕ_ν were large enough (e.g. due to microturbulence), then there may be a contribution from one or more zones. For our present discussion, however, we will assume that ϕ_ν has a narrow width (e.g. the vertical extent of the dots defining v_s in Fig. B1).

In MCs, and generally in any environment, the velocities are not discretized but rather vary continuously throughout the medium. Therefore, the velocities in Figure B1 are more accurately described by the dashed line connecting the defined v_s s in each zone. Consequently, at the observed velocity

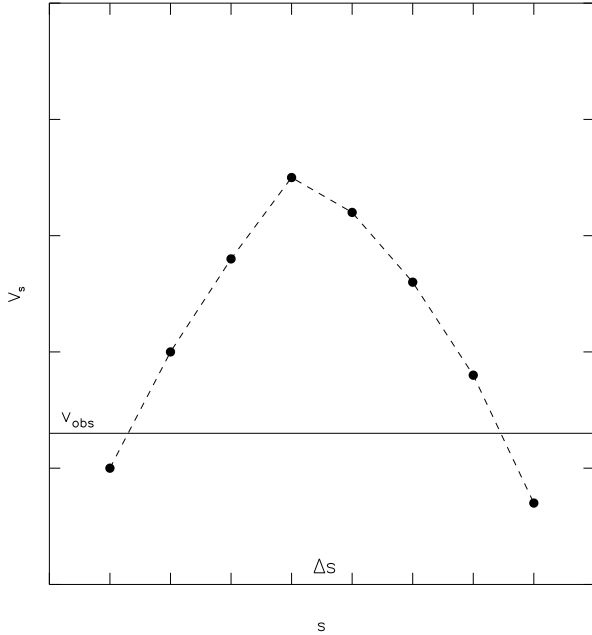


Figure B1. Velocity component along the LoS, v_s vs. s . A sample observed frequency (or velocity) is shown by the solid line, v_{obs} . The units of v_s and s are arbitrary. Due to the large velocity gradients, there would not be any observed emission at this v_{obs} , unless the velocities were interpolated (dashed line).

there would in fact be emission along this LoS, due to the overlap of v_s and v_{obs} (at two locations in this example).

In order to account for the continuous variation in cloud properties, we have implemented interpolation into our radiative transfer calculations (also see Pontoppidan et al. 2009). All the required quantities, such as temperature, CO density, H₂ density, and position, are linearly interpolated, effectively increasing the physical resolution along the LoS.

Figure B2 shows how under-sampling the velocities may produce inaccurate line profiles. The figure shows the relevant quantities from LoS A shown in Figure 15 and discussed in Section 4.5. The left panels show the results using interpolation ($16\times$ the original grid, so $\Delta s = 0.0049$ pc), and the right panels show the result using the original simulation grid ($\Delta s = 0.078$ pc). Clearly, there are stark differences in the spectra. When unresolved, the spectrum has numerous “flat tops,” and there is a sharp decrease in the intensities between -3 and -4 km s⁻¹. These features do not occur in the spectrum obtained from the interpolated LoS. The “flat tops” and intensity drop could be misidentified as saturation or absorption features, respectively, when in fact they are simply features arising due to the under-resolved grid.

The differences can be understood from the velocity and optical depth profiles. In the high density region responsible for most of the emission (see Section 4.5), there is a very large velocity gradient. At an observed velocity of -4 km s⁻¹, there would not be any emission from this region, due to the large gap in the velocities at LoS position ~ 18.5 pc. However, when interpolated (left panels), there are continuous velocities in this region, resulting in enhanced emission at -4 km s⁻¹.

For the interpolated 0.0049 pc and original 0.078 pc simulations, the integrated intensities from LoS A are 187.1 and 173.8 K km s⁻¹, respectively. This results in a slight difference of $\sim 10\%$, and would lead to a similar discrepancy in the X factor from this LoS. The precise difference would of course depend on the particular LoS – LoSs with many regions with large velocity gradients would be strongly affected by under-resolved velocities. For model n300, the cloud-average X factor is $\langle X \rangle = 2.2 \times 10^{20}$ cm⁻² K⁻¹ km⁻¹ s, regardless of whether interpolation is employed. Thus, for the n300 model, only the line shapes along individual LoS are affected by under-resolution, but the velocities are sufficiently resolved for estimating the cloud-averaged integrated intensity.

For the models discussed in Section 4.4 where we have directly modified the velocities to have larger dispersions, there will of course be large velocity gradients in adjacent zones. For these models, we find that interpolation results in more significant differences. Recall that in the altered models, the velocities are replaced in the original grid utilized in the chemo-MHD simulation. The altered velocities on this grid have the chosen dispersions. In the radiative transfer calculations, due to the large velocity gradients, interpolation leads to the addition of numerous values to the velocity dataset. In the models with large chosen dispersions in the original grid, this interpolation can potentially lead to a velocity dispersion that is different from the chosen one. For instance, in the $\sigma = 24$ and 240 km s⁻¹ models, after interpolation (with $16\times$ increased resolution), the effective velocity dispersion becomes 21 and 205 km s⁻¹, respectively. In both the $\sigma = 24$ and 240 km s⁻¹ models, we find that interpolation increases the cloud-averaged W by factors of 2 and 4 , respectively, and thereby decreases the X factor by a corresponding amount. As these models are highly artificial to begin with, we do not ensure that all the velocities are well resolved. Nevertheless, qualitatively, we can be sure that increasing the velocity dispersion leads to decreasing the X factor. As we state in Section 5.3, models of real sources with very high dispersions, such as ULIRGs, would have to be well resolved in order to quantify the X factor– σ relationship.

REFERENCES

- Ballesteros-Paredes J., 2006, MNRAS, 372, 443
- Ballesteros-Paredes J., Mac Low M.-M., 2002, ApJ, 570, 734
- Bertoldi F., McKee C. F., 1992, ApJ, 395, 140
- Bolatlo A. D., Leroy A. K., Rosolowsky E., Walter F., Blitz L., 2008, ApJ, 686, 948
- Boselli A., Gavazzi G., Lequeux J., Buat V., Casoli F., Dickey J., Donas J., 1997, A&A, 327, 522
- Boselli A., Lequeux J., Gavazzi G., 2002, A&A, 384, 33
- Burgh E. B., France K., McCandliss S. R., 2007, ApJ, 658, 446
- Combes F., 1991, ARA&A, 29, 195
- Dame T. M., Hartmann D., Thaddeus P., 2001, ApJ, 547, 792
- Dickman R. L., 1978, ApJS, 37, 407
- Dickman R. L., Snell R. L., Schloerb F. P., 1986, ApJ, 309, 326

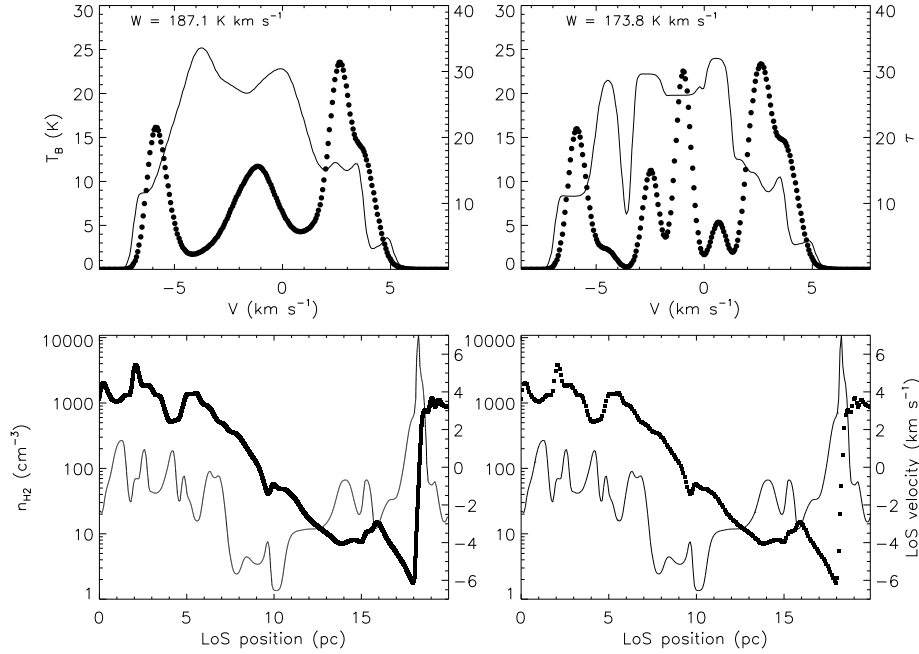


Figure B2. Spectrum, densities and velocities from LoS A (as in Fig. 15). Top panel shows the brightness temperature (lines - left axis), and integrated optical depth (circles - right axis) as a function of observed velocity. Bottom panels show density (lines - left axis) and LoS velocity (squares - right axis) as a function of LoS position. Left panels show quantities derived using interpolation, and right panels show the quantities derived directly from the original 256^3 simulation. The integrated intensities W are indicated in the top panels.

- Downes D., Solomon P. M., 1998, *ApJ*, 507, 615
Downes D., Solomon P. M., Radford S. J. E., 1993, *ApJL*, 414, L13
Draine B. T., 1978, *ApJS*, 36, 595
Gammie C. F., Lin Y.-T., Stone J. M., Ostriker E. C., 2003, *ApJ*, 592, 203
Glover S. C. O., Federrath C., Mac Low M., Klessen R. S., 2010, *MNRAS*, 404, 2
Glover S. C. O., Mac Low M., 2007a, *ApJS*, 169, 239
Glover S. C. O., Mac Low M., 2007b, *ApJ*, 659, 1317
Glover S. C. O., Mac Low M., 2011, *MNRAS*, 412, 337
Grenier I. A., Casandjian J., Terrier R., 2005, *Science*, 307, 1292
Habing H. J., 1968, *BAIN*, 19, 421
Heyer M., Krawczyk C., Duval J., Jackson J. M., 2009, *ApJ*, 699, 1092
Israel F. P., 1997, *A&A*, 328, 471
Israel F. P., de Graauw T., van de Stadt H., de Vries C. P., 1986, *ApJ*, 303, 186
Kauffmann J., Pillai T., Shetty R., Myers P. C., Goodman A. A., 2010a, *ApJ*, 712, 1137
Kauffmann J., Pillai T., Shetty R., Myers P. C., Goodman A. A., 2010b, *ApJ*, 716, 433
Kutner M. L., Leung C. M., 1985, *ApJ*, 291, 188
Larson R. B., 1981, *MNRAS*, 194, 809
Leroy A., Bolatto A., Stanimirovic S., Mizuno N., Israel F., Bot C., 2007, *ApJ*, 658, 1027
Leroy A. K., Bolatto A., Bot C., Engelbracht C. W., Gordon K., Israel F. P., Rubio M., Sandstrom K., Stanimirović S., 2009, *ApJ*, 702, 352
Leroy A. K., Bolatto A., Gordon K., Sandstrom K., Gratier P., Rosolowsky E., Engelbracht C. W., Mizuno N., Corbelli E., Fukui Y., Kawamura A., 2011, *ArXiv e-prints*
Liszt H. S., Pety J., Lucas R., 2010, *A&A*, 518, A45+
Lombardi M., Alves J., Lada C. J., 2006, *A&A*, 454, 781
Mac Low M., Klessen R. S., 2004, *Reviews of Modern Physics*, 76, 125
Maloney P., 1990, *ApJL*, 348, L9
Maloney P., Black J. H., 1988, *ApJ*, 325, 389
McKee C. F., Ostriker E. C., 2007, *ARA&A*, 45, 565
Myers P. C., Goodman A. A., 1988, *ApJ*, 329, 392
Oka T., Hasegawa T., Hayashi M., Handa T., Sakamoto S., 1998, *ApJ*, 493, 730
Pineda J. E., Caselli P., Goodman A. A., 2008, *ApJ*, 679, 481
Planck Collaboration Ade P. A. R., Aghanim N., Arnaud M., Ashdown M., Aumont J., Baccigalupi C., Balbi A., Banday A. J., Barreiro R. B., et al. 2011, *ArXiv e-prints* 1101.2029
Polk K. S., Knapp G. R., Stark A. A., Wilson R. W., 1988, *ApJ*, 332, 432
Pontoppidan K. M., Meijerink R., Dullemond C. P., Blake G. A., 2009, *ApJ*, 704, 1482
Roman-Duval J., Jackson J. M., Heyer M., Rathborne J., Simon R., 2010, *ApJ*, 723, 492
Rosolowsky E. W., Pineda J. E., Kauffmann J., Goodman A. A., 2008, *ApJ*, 679, 1338
Schöier F. L., van der Tak F. F. S., van Dishoeck E. F., Black J. H., 2005, *A&A*, 432, 369
Shetty R., Collins D. C., Kauffmann J., Goodman A. A., Rosolowsky E. W., Norman M. L., 2010, *ApJ*, 712, 1049
Shetty R., Glover S. C., Dullemond C. P., Klessen R. S., 2011, *MNRAS*, 412, 1686
Sobolev V. V., 1957, *Soviet Astronomy*, 1, 678
Solomon P. M., Downes D., Radford S. J. E., Barrett J. W., 1997, *ApJ*, 478, 144

- Solomon P. M., Rivolo A. R., Barrett J., Yahil A., 1987, ApJ, 319, 730
- Solomon P. M., Vanden Bout P. A., 2005, ARA&A, 43, 677
- Strong A. W., Bloemen J. B. G. M., Dame T. M., Grenier I. A., Hermsen W., Lebrun F., Nyman L., Pollock A. M. T., Thaddeus P., 1988, A&A, 207, 1
- Tacconi L. J., Genzel R., Smail I., Neri R., Chapman S. C., Ivison R. J., Blain A., Cox P., Omont A. e. a., 2008, ApJ, 680, 246
- van Dishoeck E. F., Black J. H., 1988, ApJ, 334, 771
- Wolfire M. G., Hollenbach D., McKee C. F., 2010, ApJ, 716, 1191
- Wolfire M. G., Hollenbach D., Tielens A. G. G. M., 1993, ApJ, 402, 195
- Yang B., Stancil P. C., Balakrishnan N., Forrey R. C., 2010, ApJ, 718, 1062
- Young J. S., Scoville N. Z., 1991, ARA&A, 29, 581